PCCP

Accepted Manuscript




ROYAL SOCIETY OF CHEMISTRY

www.rsc.org/pccp

# Morphology-controlled synthesis of monodispersed graphitic carbon coated core/shell structured Ni/NiO nanoparticles with enhanced magnetoresistance

M. Patange[1], S. Biswas[1*], A. K. Yadav[2], S. N. Jha[2], and D. Bhattacharyya[2]

[1]*Department of Physics, The LNM Institute of Information Technology, Jaipur-302031, India*

[2]*Applied Spectroscopy Division, Bhabha Atomic Research Centre, Mumbai-400085, India*

Graphitic carbon coated core/shell structured Ni/NiO nanoparticles were synthesized by a sol-gel type chemical precursor method and their structural, morphological and magnetic properties were evaluated. The synthesis method provides an improved and comparatively facile approach towards controlled growth of the composite structure of metallic ferromagnetic (FM) core and antiferromagnetic (AFM) metal oxide shell along with *in situ* growth of a supplementary surface functionalization layer of graphitic carbon. In addition, the process allows a precise control over the shape and size of this important class of core/shell type functional materials for a wide range of pertinent applications. The structural properties of the derived samples were studied with X-ray diffraction (XRD), X-ray absorption near edge structure (XANES), extended X-ray absorption fine structure (EXAFS), Raman spectroscopy, energy dispersive X-ray (EDX) analysis, and X-ray photoelectron spectroscopy (XPS). The microstructural features in the core/shell structured particles were evaluated with scanning electron microscope (SEM) and high resolution transmission electron microscope (HRTEM). Magnetic properties of the derived samples were studied with a vibrating sample magnetometer (VSM) in the 80-300 K temperature range. The surface functionalized Ni/NiO nanoparticles exhibit a distinctly enhanced magnetoresistance (MR), *e.g.*, -10% at 290 K, than reported values in compacted Ni/NiO powders or composites.

**Keywords :** Core/shell, Ni nanoparticles, Graphitic carbon, Ferromagnetism, Surface functionalization.

*Corresponding author. Tel : +91-7597171575, Fax : +91-141-2689014

E-mail : drsomnathbiswas@gmail.com

## Introduction

Core/shell structured nanoparticles have received considerable attention in recent past owing to their physical and chemical properties that are strongly dependent on the structure of the core, shell, and their interface.[1-5] This structure dependence opens possibilities for tuning properties by controlling their chemical composition and relative size of the core and shell. The core/shell structured magnetic nanoparticles are of special interests since such heterogeneous nanostructures are potentially attractive for developing devices and cluster-assembled materials with wide functionalities.[6-8] The nonmagnetic, antiferromagnetic, or ferro/ferri-magnetic shell layer in such magnetic nanoparticles serves various functions. The shell structure not only provides a stabilization layer to the magnetic core but also a platform for surface functionalization of the nanoparticles.[9,10] Nanoparticles composed of magnetic cores with continuous metallic shell layers simultaneously possess both magnetic and plasmonic properties.[11,12] Small sized superparamagnetic core/shell structures with suitable biocompatible coatings have importance in biology, biotechnology, and other biomedical disciplines.[10,13] Renewed interest has recently been shown in core/shell exchange-bias (EB) systems due to their potential application in increasing the superparamagnetic limit of small magnetic nanoparticles used in magnetic read heads and similar systems, and prospective future application in magnetic random access memory (MRAM).[14-16] In core/shell type FM/AFM nanostructures, the first system seen to exhibit EB,[2,4] the AFM shell layer can be effectively designed to tune the resultant magnetocrystalline anisotropy of the FM metal cores for long term thermal stability. Recent studies have provided added insight into the possible origins of exchange anisotropy in such type of core/shell nanoparticles, however, the geneses of the experimentally observed diverse behaviors are still an unsolved problem.[15,16] In Ni/NiO nanoparticles, the AFM NiO layer promotes an enhancement in the magnetic anisotropy (exchange anisotropy) of the FM core and the stabilization of the orientation of FM moment before thermal energy (at high temperatures) source the fluctuating orientations of magnetic moments.[7,11] Moreover, the Ni/NiO core/shell nanoparticles are reported to have spin dependent MR properties, making it a rare example showing a metallic conduction mechanism and exhibiting both EB and MR effects well-matched in a single system.[17-21] The MR phenomenon in such granular systems crucially depends on the structural parameters, in particular the concentration and size distribution of the FM cores and their inter-distances. The spin glass like NiO component at the periphery of the Ni nanoparticles

supports the coexistence of EB and MR in such systems. As expectedly, the MR effect in these samples is largely affected by the exchange anisotropy and can be possibly adjusted by modifying the magnetic configuration of the core/shell structure. Compared to Ni/NiO core/shell nanoparticles, other magnetic metal/metal oxide systems such as Co/CoO and Fe/FeO, also show large EB, but their low Neil temperatures ($T_N$) (CoO ~290 K and FeO ~198 K) severely limits their potential use in devices operated at/above room temperature.[11,22] In contrast, high $T_N$ ~520 K of NiO makes it a prominent candidate for producing useful EB at room temperature.

Beyond the magnetism, there are substantial interests in Ni nanoparticles and the oxides of Ni for novel applications, *e.g.*, growing carbon nanotubes and nanofibers,[23,24] catalysts in chemical reactions,[25] hole transport layer in LEDs,[26] *etc.* The Ni/NiO nanoparticles are also highly attractive for electrochemical energy storage and conversion.[27-29] Due to its high capacity and low cost, NiO is considered as a promising candidate material for anode in lithium ion batteries. The combination of metallic Ni with NiO accelerates the charge transfer process and reduces polarization resulting in improved rate capability and cycling performance.

However, the development of a tunable core/shell microstructure of magnetic nanoparticles with reproducible tailored properties is very much intricate in nature and presents a great defy to the scientific community.[4,22,30] The physical properties of such core/shell structures could be hardly tuned with high reproducibility, unless a convenient method of modifying the magnetic and structural configuration is envisaged. Fine control over the Ni/NiO core/shell microstructure including their interfacial properties, and the concentration and distribution of Ni present in the highly ordered Ni/NiO lattices are of utmost necessity to tailor their properties. The frequently encountered obstacle in nascent Ni nanoparticles is the spontaneous and uncontrolled growth of the NiO shell layer.[4,30] Controlled oxidation of Ni in ambient air is an exigent phenomenon, owing to the high reactivity of metallic Ni with oxygen and the availability of diverse nickel oxide stoichiometries. Therefore, a convenient synthesis technique of such an important class of material is highly crucial for efficient and controlled tailoring of the core/shell microstructure in the samples to achieve the desired properties. Furthermore, the method must be viable for mass scale production at an economic cost, highly reproducible in nature as well as environmentally benign. In literature, there are many recent reports on the

development of Ni/NiO core/shell nanostructures by different techniques including pulsed laser deposition,[1,7] thermal decomposition,[4,25] solution-phase synthesis,[11,13] electrostatic spray deposition,[27] microwave assisted synthesis,[31,32] chemical co-reduction,[33,34] mechanical milling,[35,36] high temperature oxidation-reduction process,[37] magnetron sputtering,[38] laser irradiance,[39] and electrodeposition methods.[29,40] The large volume of published literature in the recent past reflects the importance of Ni/NiO nanostructures and the humongous efforts being made to tailor their properties for optimum performance. Few of these highly attractive approaches show prominent and effective designs of Ni/NiO nanostructures for scaled-up use in industrial processes.

Among the various techniques followed for the synthesis of Ni/NiO core/shell nanoparticles, the chemical synthesis methods are one of the most prominent and comparatively facile approaches for the production of the samples in the form of fine powders. Thakur *et al* [41] described a sol-gel route to produce Ni/NiO core/shell nanoparticles using nickel nitrate and citric acid. Harraz *et al* [42] also reported a sol-gel type method for the development of Ni/NiO nanoparticles using $Ni(NO_3)_2.6H_2O$, citric acid and pure alcohol. Similarly, Karimipour *et al* [43] synthesized Ni/NiO nanoparticles embedded in $TiO_2$ following a complex polymer based sol-gel method. However, the development of Ni/NiO nanoparticles with a controlled microstructure via chemical synthesis routes is very much challenging in nature and has certain limitations. Few of these limitations must be fully addressed to ensure the applicability and reliability of these high-end materials for use in state of the art applications. Improvements are needed in (i) regulating the uniformity and stability in shape and size of the core/shell type nanostructured materials, (ii) tailoring the magnetic, electrical, and optical properties of the materials by effective control over the core/shell microstructure, and (iii) formulating a convenient and reproducible method for mass-scale production of Ni/NiO and a series of similar type of magnetic core/shell structures. In this regard, the present low-temperature technique provides efficient control over the morphology of the core/shell type magnetic nanoparticles with excellent reproducibility, and inducing relevant magnetic, electrical, and optical features for pertinent applications in wide areas including spintronics, magneto-optics, magnetic memory devices, biosensors, drug delivery, gas sensors, catalysis in chemical reactions, and stem-cell differentiation and imaging.

## Experimental section

### Synthesis of graphitic carbon coated Ni/NiO core/shell nanostructures

The materials used in this synthesis process were nickel nitrate hexahydrate [$Ni(NO_3)_2.6H_2O$, mol. wt. = 290.81, Sigma Aldrich, 99.99% pure], *poly*-vinyl alcohol (PVA) [mol. wt. ~96800, degree of polymerization ~2000, Fisher Scientific], 25% ammonia solution ($NH_4OH$, conc. 25%, Merck), and sucrose ($C_{12}H_{22}O_{11}$, mol. wt. = 342.30, Merck, 99.95% pure). All the reactants were used without any further purification.

The synthesis method involves the steps of (a) preparing aqueous solutions of nickel nitrate hexahydrate, PVA and sucrose, (b) dispersing the $Ni^{2+}$ ion solution in small amounts in the PVA-sucrose polymer molecules, (c) enclosing the $Ni^{2+}$ ion clusters inside the PVA-sucrose polymer micelles in a rather stable form, and then (d) aging of the precursor in air at room temperature or lower. The reaction process is described in detail below.

A drop wise addition of $Ni(NO_3)_2.6H_2O$ (in 0.2 M solution) to a mixed PVA-sucrose solution (in 1 : 10 ratio by mass) in water at 60-65°C with continuous magnetic stirring results in a homogeneous dispersion of the salt ions in the polymer micelles. The sucrose additive, used in this method, improves average viscosity of the reaction solution such that the PVA-sucrose polymer micellar wall behaves to be rather stable and does not pile off so easily during the reaction. It was observed that the reaction of the salt solution with the PVA-sucrose molecules was endothermic in nature. During the reaction, $p^H$ of the mixed solution was maintained at ~9 by adding required amount of $NH_4OH$ solution to support the hydrogenation of $Ni^{2+}$ ions in the reaction solution. The reaction proceeded with a successive change in average colour of the resulting solution from characteristically *spring greenish*, just after the addition of the Ni salt solution in the transparent colorless PVA-sucrose solution, to a *jungle greenish* one and then finally after ~30 min, to a *persian greenish* one along with the formation of a turbid *persian greenish* colour precipitation. The changes in the reaction solution during the process were studied with *in situ* measurement of UV-visible absorption characteristics of the reaction solution, which confirmed the nucleation of NiO phase in the reaction solution.

After the reaction, the solution was cooled to room temperature (290 K) and aged for 24 h to convert it into a gel. A fluffy voluminous *persian greenish* colour mass of polymer capped precursor powders was obtained after drying the gel at a controlled temperature of

50-60°C in air. Recrystallized core/shell type Ni/NiO nanoparticles in the form of finely divided loose powders were obtained by heat treating the polymer capped precursor powders, after pulverizing by grinding with a mortar and pestle, at selected temperatures in the range 400-900°C in ambient air for 2 h. The heat treatment temperature is decisive in controlling the final size of the nanoparticles.

### Structural, microstructural and magnetic characterization

The crystalline nature of the derived samples were analyzed with a Panalytical X`Pert Pro X-ray diffractometer using $CuK_{\alpha}$ radiation of wavelength 0.1545 nm, employing at a scanning rate of 0.02/s. Raman measurements were carried out with Horiba Jobin Yvon LabRAM HR800 spectrometer with an He-Ne laser source (632.8 nm). FESEM images and EDX data of the samples were obtained with FEI Quanta FEG-200 microscope, at an accelerating voltage of 20 kV. A more close-up view of such images was studied at 200 kV by a JEOL JEM-2100 HRTEM. The X-ray absorption measurements were carried out in the dispersive EXAFS beamline (BL-8) of the INDUS-2 Synchrotron Source (2.5 GeV, 100 mA) in transmission mode at Raja Ramanna Centre for Advanced Technology (RRCAT), Indore, India.[44,45] The surface structure of the derived nanoparticles was studied in terms of the XPS bands, recorded with a Shimadzu AXIS Ultra spectrometer by exciting the samples under a reduced pressure ~$10^{-8}$ Pa, with Mg $K_{\alpha 1,2}$ radiation of 1253.6 eV energy operating at 12 kV and 20 mA. The magnetic properties were measured with a LakeShore 74046 VSM with applied magnetic fields up to 20 kOe in the 80-300 K temperature range. The MR properties were further analyzed with a Keithley 2400 SourceMeter and an electromagnet (Model HEM-100) of Polytronic Corporation, India.

## Results and discussion

### Reaction mechanism and growth process of $Ni^{2+}$-PVA-sucrose chelate complex

As described elsewhere,[46,47] while stirring in an aqueous solution at 60-65°C temperature, the dispersed PVA molecules experience thermo-mechanical stretching and form small groups or micelles in the shape of laminates or closed ring. Such micelles have plenty of OH groups free from H-bonding, *i.e.*, active molecules of extended molecular surfaces, useful to support a surface-activated reaction of interest. A micelle of such PVA molecules isolates itself from the surrounding in the solution according to its interfacial surface tension. As a result, such an array

of PVA micelles so obtained in the solution behave as surfactants and adsorb the $Ni^{2+}$ cations at the surface while adding the salt solution, forming a metal ion-polymer chelate complex. Successive changes observed in initial $Ni^{2+}$-PVA-sucrose colour infer a dynamic reaction in operation in divided reaction centers in the solution. The chelate structures render a self-controlled redox reaction with the active $OH^-$ groups and finally form a stable $Ni^{2+}$-PVA-sucrose product in the colloidal solution. Mobile $Ni^{2+}$-PVA-sucrose chelates, under hot conditions in the solution, serve as active reaction species to react with one another in small groups of micelles. As a result, the $Ni^{2+}$ nucleates and grows with a peculiar Ni-core-NiO-shell structure within the polymer micelles, depending on the $Ni^{2+}$ concentration, dispersion and other experimental conditions. Aging at room temperature, following the reaction, causes a surface stabilized Ni/NiO core/shell nanostructure by interbridging of a specific surface structure via PVA-sucrose molecules. During the subsequent heat treatment, the PVA-sucrose surface layer transforms into a rigid thin layer of graphitic carbon of few nanometer thickness on the recrystallized Ni/NiO nanoparticles.

Chemically, the addition of $Ni^{2+}$ salt solution in the basic PVA-sucrose solution initiates the formation of nickel hydroxide in the solution. This is manifested in the instantaneous formation of a turbid *persian greenish* colour precipitation in the reaction solution. The nickel hydroxide precipitate is soluble in the basic medium ($p^H \sim 9$), producing nickel oxide anions (nickelates), which are trapped in the polymer micelles and after aging, nucleate to produce the stable Ni/NiO core/shell type nanoparticles of controlled shape and size.

The reactions involved are,

$$(Ni^{2+} + 2NO_3^{2-}) + 2(NH_4^+ + OH^-) \rightarrow Ni(OH)_2 + 2NH_3\uparrow + 2HNO_3 \qquad (1a)$$

$$Ni(OH)_2 + 2(NH_4^+ + OH^-) \rightarrow NiO_2^{2-} + 2NH_3\uparrow + H_2\uparrow + 2H_2O \qquad (1b)$$

$$\downarrow$$

Ni/NiO core/shell nanoparticles

It has been observed that a $p^H \sim 9$ is necessary for the controlled growth of the nanoparticles in the polymer micelles and is highly decisive in determining the morphology of the final products. Further increase in the $p^H$ level leads to a competition between the growth and erosion of the nascent metal oxide nanoparticles in the polymer micelles, affecting the effective growth rate and final morphology of the particles.

**Structure and morphology**

Fig. 1 compares the XRD patterns of graphitic carbon coated core/shell structured Ni/NiO nanoparticles derived after heating the $Ni^{2+}$-PVA-sucrose precursor powders in ambient air for 2 h at (a) 400°C, (b) 450°C, (c) 500°C, and (d) 600°C, respectively. The sample (a) shows five broad distinctive peaks corresponding to (111), (200), (220), (311), and (222) crystalline planes of NiO (JCPDS card 04-0835) and two weak and broad peaks corresponding to the (200) and (220) planes of Ni (JCPDS card 04-0850). With the increase in the heat treatment temperature, all the XRD peaks become sharper and narrower with a drastic decrease in the relative intensity of the NiO peaks in comparison to the Ni peaks. The gradual increase in intensity of the Ni peaks with the increase in heat treatment temperature clearly reflects the increase in Ni content in the core-shell type particles. The broad and intense NiO (200) peak in sample (a) splits into two distinctive peaks corresponding to NiO (200) and Ni (111) in sample (b). As can be seen in sample (c) and (d), the NiO peaks gradually diminish with further increase in heat treatment temperature and the Ni peaks corresponding to (111), (200), and (220) planes become more intense and sharp. The lattice constant $a$, lattice volume $V_0$, density $\rho$ and average crystallite size $d$ derived from the diffractograms are given in Table 1. In all the samples, both Ni and NiO phases have face-centered cubic (*fcc*) crystal structure with *Fm-3m* space group. A bit larger $a$-value of Ni, *viz*, 0.3540 nm in sample (a) or 0.3538 nm in sample (d), lies in comparison to a value of 0.3523 nm in bulk Ni (JCPDS card 04-0850). This corresponds to $V_0 = 0.0446$ nm$^3$ ($\rho$ = 8.79 g/cc) in sample (a) or 0.0442 nm$^3$ ($\rho$ = 8.80 g/cc) in sample (d), with Z = 4 units, in comparison to $V_0 = 0.0437$ nm$^3$ ($\rho$ = 8.91 g/cc) in bulk Ni (JCPDS card 04-0850). Similarly, the NiO phase shows a larger $a$-value, *viz*, 0.4196 nm in sample (a) or 0.4192 nm in sample (d), in comparison to 0.4177 nm in bulk NiO (JCPDS card 04-0835). This corresponds to $V_0 = 0.0738$ nm$^3$ ($\rho$ = 6.71 g/cc) in sample (a) or 0.0736 nm$^3$ ($\rho$ = 6.73 g/cc) in sample (d), with Z = 4 units, in comparison to $V_0 = 0.0728$ nm$^3$ ($\rho$ = 6.81 g/cc) in bulk NiO (JCPDS card 04-0835). The lattice expansion in nanoparticles has been attributed to a number of possible phenomena including size confinement effects, grain surface relaxation, formation of point defects, and uncompensated Coulombic interactions.[4,48,49] However, in the present samples, the observed ~ 0.5% increase in

the $V_0$ values of Ni and NiO over that of their bulk counterparts is predominantly due to the core-shell structure of the particles.[47,50] The core-shell structure is responsible for the interfacial interactions (interface between Ni and NiO, and NiO and graphene). This kind of interaction causes two types of strains in the lattice.[47,51,52] One is the macrostrain, which increases the interplanar spacings ($d_{hkl}$), and the other is the microstrain, which induces a peak broadening. As expected, the size of Ni and NiO crystallites (*d* values), calculated from the Debye Scherrer relationship[51] using the full width at half-maximum (*fwhm*) in the peaks, show gradual increase with the increase in heat treatment temperature of the samples.

In such small Ni/NiO core-shell type particles, a slightly modified intensity distribution of X-ray diffraction peaks lies in comparison to reported distribution in bulk Ni and NiO. Nevertheless, in either case, (111) reflection lies as the most intense peak in the Ni core, with the second and third most intense peaks of (200) and (220) reflections, respectively. Assuming a normalized value of peak intensity $I_p$ = 100 units in (111) peak of sample (d), a value of $I_p$ =36 units lies in (200) peak while of 17 units in (220) peak in comparison to the values of 42 and 21 units, respectively, in bulk Ni (JCPDS card 04-0850). Similarly, the (200) reflection lies as the most intense peak in the NiO shell as in bulk NiO, with the second and third most intense peaks of (111) and (220) reflections, respectively. Assuming a normalized value of peak intensity $I_p$ = 100 units in (200) peak of sample (a), a value of $I_p$ = 53 units lies in (111) peak while of 43 units in (220) peak in comparison to the values of 91 and 57 units, respectively, in bulk NiO (JCPDS card 04-0835). Further analysis of the XRD data was performed with PowderCell 2.4 program,[53,54] to estimate the relative concentration of Ni and NiO phases in the core/shell structured nanoparticles. As given in Table 1, the Ni concentration in the derived samples monotonically increased (NiO concentration monotonically decreased) with the increase in the processing temperature. The sample (a) has a concentration (at.%) of Ni and NiO of 8.8% and 91.2%, respectively, which get changed to 47.2% and 52.8%, respectively in sample (d).

Fig. 2 shows the normalized XANES spectra of Ni/NiO samples processed at different temperatures along with NiO and Ni standard samples. The normalized XANES spectra show the plot between absorption coefficient $\mu(E)$ as a function of photon energy *E*. XANES structure is sensitive to the oxidation state and chemical environment of the central atom. It can be observed that as the heat treatment temperature increases the absorption edge of the derived samples

moves towards Ni edge and lie in between the Ni and NiO edges which is an indication of the presence of mixed oxidation state of Ni ($Ni^{o}$ and $Ni^{2+}$). However, the sample derived at 400°C shows an anomalous behavior of shifting slightly towards higher energy side, possibly due to the existence of $Ni_2O_3$ along with the major phases of Ni and NiO.[55-57] To quantitatively estimate the relative amount (vol.%) of the two phases in the samples, the XANES spectrum of each sample was fitted with a linear combination of the XANES spectra of a pure Ni foil and a standard NiO sample. Figs. 2b-c show such linear combination fit of the two representative samples processed at 500°C and 600°C, respectively. It has been observed from the above exercise that as the heat treatment temperature increases from 500°C to 600°C, the NiO content in the sample reduces from 70% to 55%.

To take care of the oscillations in the absorption spectra, $\mu(E)$ has been converted to absorption function $\chi(E)$ defined as follows,[58]

$$\chi(E) = \frac{\mu(E)-\mu_0(E)}{\Delta\mu_0(E)} \quad (2)$$

where, $E_0$ is the absorption edge energy, $\mu_0(E)$ is the bare atom background and $\Delta\mu_0(E)$ is the step in $\mu(E)$ value at the absorption edge. The energy dependent absorption coefficient $\chi(E)$ has been converted to the wave number dependent absorption coefficient $\chi(k)$ using the relationship,

$$k = \sqrt{\frac{2m(E-E_0)}{\hbar^2}} \quad (3)$$

where, $m$ is the electron mass and $\hbar$ is the reduced Plank's constant. After background subtraction, the EXAFS spectra are plotted in the $k$ range of 0-9 $Å^{-1}$. Fig. 3a shows the $k$-space spectra for all the samples along with NiO and Ni standards. As can be observed, the spectrum corresponding to the $Ni^{2+}$-PVA-sucrose precursor is broadly different from the NiO and Ni standard spectra. The $k$ space spectrum of the sample heated at 400°C is nearly similar to that of standard NiO. As the heat treatment temperature increases, the spectral features around 5.25 $Å^{-1}$ and 8.25 $Å^{-1}$ start appearing and the feature around 6 $Å^{-1}$ starts diminishing. $\chi(k)$ is weighted by $k$ to amplify the oscillation at high $k$ and the $k.\chi(k)$ functions are Fourier transformed in $R$ space to generate the $\chi(R)$ versus $R$ spectra in terms of the real distances from the center of the absorbing atom. The set of EXAFS data analysis available in IFEFFIT software package was used for the EXAFS data analysis.[59] This includes background reduction and Fourier transformation to derive the $\chi(R)$ versus $R$ spectra from the absorption spectra (using ATHENA

subroutine), generation of the theoretical EXAFS spectra starting from an assumed crystallographic structure (using ATOMS subroutine) and finally fitting of experimental data with the theoretical spectra (using ARTEMIS subroutine). The $\chi(R)$ versus $R$ spectra were generated for all the samples from the $\mu(E)$ versus $E$ spectra following the methodology described above and the best fit $\chi(R)$ versus $R$ spectra of the samples are shown in Fig. 3b along with the experimental data for all the samples. To generate theoretical model, we have used NiO rock salt structure for the samples treated at 400°C and 450°C. However, for the samples treated at 500°C and 600°C, we have included Ni *fcc* structure first shell to improve our fit. The bond distances R, co-ordination numbers N (including scattering amplitudes) and Debye-Waller disorder factors ($\sigma^2$), which give the mean square fluctuations in the bond distances, have been used as fitting parameters. The best fit results are summarized in Table 2.

From the Fourier transformed EXAFS spectra, shown in Fig. 3b, it can be observed that the first peak of Ni-O shell for the samples treated at 400°C has similar amplitude as that of pure NiO sample. As the heat treatment temperature increases, the first shell peak amplitude starts decreasing. This effect is also reflected in the fitting results (Table 2). The Ni-Ni metallic shell starts contributing as the heat treatment temperature increases. The results obtained from EXAFS fitting also shows that metallic Ni contribution starts increasing as the heat treatment temperature increases. The above observations agree with the absorption edge shifts in the XANES spectra of the samples.

Similar X-ray absorption behavior in Ni/NiO samples is also reported. For example, Bianco *et al*[35] prepared NiO/Ni core/shell type structures by ball-milling of NiO powders, followed by annealing in hydrogen atmosphere. It was observed that with increasing annealing temperature the local structure gradually changes from typically rock salt structure to *fcc* Ni structure. Zhou *et al*[60] observed the presence of mixed NiO and Ni phases from the XANES measurements at Ni K edge, when Ni layers grown by magnetron plasma based cluster beam deposition techniques, are subjected to oxygen feeding. Migowski *et al*[61] synthesized Ni nanoparticles by decomposing an organometallic precursor, bis(1,5-cyclooctadiene) nickel(0) dispersed in 1-alkyl-3-methylimidazolium N-bis(trifluoromethanesulfonyl) amide ionic liquids. EXAFS analysis of the Ni nanoparticles dispersed in the ionic liquids showed very low values of coordination numbers. It was concluded from the analysis that NiO phase is present along with Ni in the ionic liquids.

Local structure and its relaxation around Ni atoms in nanocrystalline NiO were also studied with Ni K-edge X-ray absorption spectroscopy by Anspoks and Kuzmin.[62] It was concluded from the analysis that the lattice in nano-NiO is expanded as compared to bulk NiO.

Fig. 4 shows the typical SEM microstructure of the derived Ni/NiO core/shell nanoparticles obtained after heating the precursor powders at (a) 500°C and (b) 600°C, respectively. As can be observed in both micrographs, extremely tiny Ni/NiO nanoparticles formed marigold flower like loose clusters of spherical shape in recombination reaction in small crystallites during the processing. A close up view of the clusters reveals the tiny nanoparticles of 10-20 nm size. The clusters have a typical size of 30-100 nm. The few bigger agglomerates have grown in recombination of 2-3 such clusters. Similar microstructure is observed in other samples in this series. The elemental composition of the core/shell type nanoparticles derived at 500°C is shown in Fig. 4c. The EDX spectrum confirms the presence of the elements C, Ni and O in the samples. A quantitative measurement suggests an atomic content of 10.60%, 46.96%, and 42.44% respectively of these three elements. As expected, the Ni and O are the major elements in the core of the particles coated with the thin surface layer of carbon. In the samples derived at 400°C (not shown here), the atomic content of these three elements are 20.06%, 35.31% and 44.63%, respectively. Increased heat treatment temperature reduced the carbon layer followed by an atomic redistribution in the core containing Ni and O.

Monodispersed Ni/NiO core/shell nanoparticles of almost spherical shape and a narrow size distribution can be observed in the HRTEM images in Fig. 5. The average size of the particles are 5 nm and 10 nm in the samples derived at 400°C (Fig. 5a) and 500°C (Fig. 5b), respectively. The size of the particles in the samples derived at 400°C, matches well with the *d*-value of Ni derived from the XRD analysis (Table 1). The magnified view of a particle (inset of Fig. 5b) shows the finer details of the core/shell architecture with the Ni core diameter and NiO shell thickness of 5 nm and less than 2 nm, respectively. These values in the sample derived at 500°C are smaller than the corresponding *d*-values of Ni and NiO (Table 1). Further magnification reveals the crystalline planes in the highly dispersed particles (derived at 500°C) as shown in Fig. 5c. The well-defined lattice fringes were identified to be from two distinct domains: the spacing of 0.24 nm corresponding to the lattice-resolved (111) crystalline plane of NiO shell, and the fringes with the lattice spacing value of 0.20 nm from the (200) facets of Ni core. Fig. 5d shows a typical SAED pattern corresponding to the samples derived at 500°C, consisting of six

distinct concentric rings with discontinuous spots over the rings. As marked therein, the rings with $d_{hkl}$ values of 0.2432, 0.2080, and 0.1449 nm appear due to reflections from (111), (200) and (220) planes of the NiO shell, and the rings with $d_{hkl}$ values of 0.2069, 0.1755, and 0.1276 nm appear from the (111), (200) and (220) planes of the Ni core of the composite structure. These $d_{hkl}$ values match well with the values derived from XRD analysis.

Raman and XPS analyses were performed to characterize the surface structure of the Ni/NiO core/shell nanoparticles. Fig. 6 shows the Raman spectra of the derived Ni/NiO core/shell nanoparticles after heating the precursor powders at (a) 400°C, (b) 500°C and (c) 600°C for 2 h in ambient air. Due to strong resonance Raman scattering in graphene-based materials,[63-66] Raman spectroscopy has been extensively employed to characterize graphitic materials in recent years.[67-69] Pristine graphene shows a single sharp peak of G band at ~1580 $cm^{-1}$, which corresponds to the vibration of $sp^2$ carbon. In graphene oxide, the G-band blue-shifts to ~1590 $cm^{-1}$ and becomes broader compared to graphene, and a new broad and intense peak of D-band appears at ~1330 $cm^{-1}$, which corresponds to $sp^3$ carbon and defects associated with vacancies and grain boundaries.[67-70] As can be observed in Fig. 6, all the three samples show two broad and intense peaks corresponding to D and G bands. These bands in the Raman spectra originating from the breathing mode of the phonons of $A_{1g}$ symmetry (D band ~1330 $cm^{-1}$ for graphene oxide) and the first-order scattering of $E_{2g}$ mode (G band ~1580 $cm^{-1}$ for pristine graphene) are confirming the presence of graphitic carbon on the surface of the Ni/NiO nanoparticles.[68,71] The large *fwhm*-values of the two peaks in the samples also suggest that the graphitic carbon layer is extremely thin (few nm) in size.[72] The G-band positions in the three samples derived at 400°C, 500°C and 600°C, are 1588 $cm^{-1}$, 1588 $cm^{-1}$, and 1597 $cm^{-1}$, respectively. The observed shift of the G band in the samples indicates a weak interaction and subsequently a charge transfer between the graphitic carbon layer and the Ni/NiO nanoparticles.[73] Moreover, it is quite probable that the top surface of the graphitic layer is getting further oxidized with the increase in processing temperature. The D-band positions in the three samples are 1354 $cm^{-1}$, 1360 $cm^{-1}$, and 1351 $cm^{-1}$, respectively. The gradual decrease in the intensity of the D and G bands with the increase in heat treatment temperature is associated with the change in thickness of the carbon layer on the surface of the particles. The intensity ratio of D to G bands ($I_D/I_G$) can be used to study the structural properties of this carbon layer. As reported elsewhere,[74,75] the $I_D/I_G$ ratio is related to the amount of disorder or the size of the $sp^2$ domains. In all the three samples, the

intensity of D band is lower than that of the G band with an $I_D/I_G$ value in the range of 0.84-0.88, indicating a relatively ordered and highly graphitized structure. Similar values were reported by Wu *et al*[76] in carbon coated NiO core/shell ($I_D/I_G$ = 0.90) and carbon coated Ni/NiO core/shell hybrid ($I_D/I_G$ = 0.78) nanoparticles. In addition to the graphitic carbon bands, the presence of NiO phase in the derived samples is confirmed by the two peaks appeared at 510 and 678 $cm^{-1}$. The broad peak near 510 $cm^{-1}$, appeared in all the three samples is attributed to the first order longitudinal optical (LO) mode of NiO.[27,73,76] The second order longitudinal optical (2LO) mode observed at ~ 678 $cm^{-1}$ in the sample derived at 400°C, almost diminished in the samples derived at higher temperatures. However, the frequently observed transverse optical (TO) or mixed TO + LO modes (near 375 $cm^{-1}$ and 1085 $cm^{-1}$, respectively) of NiO are not well defined in these graphitic carbon coated Ni/NiO nanoparticles.

Similar to Raman spectroscopy, the XPS is a very sensitive analytical probe for studying the surface features down to a few atomic layers from the top surface of the particles. We applied it here to substantiate the results obtained from Raman spectroscopy on the typical structure of the graphitic carbon coated Ni/NiO core/shell nanoparticles. A survey XPS spectrum in the 0-600 eV binding energy ($E_b$) range of the samples derived at 400°C is shown in Fig. 7a. As expected, in addition to a strong characteristic O1s band, it includes intense C1s band and relatively weaker 3p and 3s Ni-bands from the Ni/NiO core/shell type nanoparticles covered with a surface carbon layer in a specific structure. For further analysis of the surface structure, the C1s, O1s and Ni3p bands were deconvoluted into their component bands.

As shown in Fig. 7b, the O1s band in the graphitic carbon coated Ni/NiO nanoparticles appears as a triplet after deconvolution with the bands shown at 529.8 eV, 531.9 eV and 533.9 eV. The intense and broad primary peak at 529.8 eV is close to the reported O1s band at 529.0 eV in pristine NiO.[73,77] In comparison to pristine NiO, a 0.8 eV increase in the O1s band in the core-shell structure is the result of a locally modified $O^{2-}$ state in bridging with graphitic carbon at the surface (possibly forming a Ni-O-C bond).[73,78] The second most intense band at 531.9 eV is primarily originating from the C=O bonds in the interfacial region between NiO and graphitic carbon.[79] Partial contributions are possibly from residual oxygen containing groups such as –COOH or -OH bonded with the surface C atoms. Wu *et al* reported such band at 531.5 eV in $Fe@Fe_2O_3$-graphene hybrid composites.[80] The weak band at 533.9 eV is assigned to C-OH bonds possibly from the undesired oxygen species on the surface of the graphitic carbon coated

Ni/NiO nanoparticles.[81,82] Similarly in Fig. 7c, the deconvoluted C1s band reveals three components, the main component lying at 285.1 eV, the second component at 287.6 eV (*i.e.*, 2.5 eV higher to the main peak), and the third component at 289.2 eV (*i.e.*, 4.1 eV higher to the main peak), indicating the complex chemical environment in the surface carbon layer of the Ni/NiO nanoparticles. The intense and broad deconvoluted band at 285.1 eV is attributed to the $sp^2$ hybridized graphitic carbon bonded to NiO and carbon with defects.[83,84] This defect peak is generally observed with an energy difference of 0.2-1.5 eV relative to the reported value of $sp^2$ (284.3 eV)[85] hybridized graphitic carbon and quite often mistakenly considered as C-C ($sp^3$) bond. The C-C ($sp^3$) band is reported at 285.1 eV in nano-diamond films and amorphous carbon.[86] In correlation with the observed Raman spectra, we conclude that the observed shift (0.8 eV) in the $sp^2$ hybridized graphitic carbon is possibly originating from the enhanced graphene domain edges and other defects formed while bonding with the NiO layer.[87] The two weak bands located at 287.6 eV and 289.2 eV correspond to C=O and –COOH groups, respectively.[88,89] As mentioned before, the C=O bond is formed in the interfacial region between NiO and graphitic carbon. The appearance of –COOH group is indicating the adsorption of oxygen species on the surface of the graphitic carbon coated Ni/NiO nanoparticles.

Fig. 7d shows the deconvoluted Ni 3p band with a doublet structure at 68.02 eV and 73.4 eV. The intense and broad deconvoluted peak at 68.02 eV is attributed to the $Ni^{2+}$ state of NiO.[90,91] The weaker peak at 73.4 eV is ascribed to $Ni_2O_3$,[90,92] possibly originating from a $Ni^{2+} \rightarrow Ni^{3+}$ transition at the interfacial layer between NiO and graphitic carbon. In fact, this peak is revealing the active interfacing between the two layers near the particle surface. As mentioned before, the presence of $Ni_2O_3$ was also determined by XANES in the samples derived at 400°C. However, no signature of $Ni_2O_3$ was found in the XRD data.

A model structure of a Ni/NiO core/shell nanoparticle with a surface layer of graphitic carbon is proposed in Fig. 7e based on the observed XPS and Raman bands in selected atoms primarily from the surface regions. While the top layer contains mostly neutral carbon atoms in the graphitic structure, part of the carbon atoms in the bottom layer chemically bond to the $O^{2-}$ species from the NiO layer in forming a cross-linked structure. As inferred from the XRD and Raman results, the dimension of the Ni core, and the thickness of the NiO and graphitic carbon shells get changed with the change in heat treatment temperature. The samples prepared at 600°C

have a larger Ni core and thinner NiO and carbon shell layers in comparison to the samples derived at lower temperatures.

**Magnetic behavior**

To investigate the role of the typical microstructure on the magnetic properties of the derived samples, magnetization measurements of the graphitic carbon coated Ni/NiO core/shell nanoparticles were carried out in 20-300 K temperature range. Fig. 8 shows the room temperature magnetic hysteresis curves (*M-H*) of the graphitic carbon coated Ni/NiO core/shell nanoparticles derived after heating the precursor powders at selected temperatures. The magnetic parameters derived from the hysteresis loops are given in Table 1. As can be observed, the saturation magnetization ($M_S$) and remanence ($M_R$) in the derived samples increased with the increase in heat treatment temperature in the 400-600°C range, which can be definitely attributed to the increase in Ni content (decrease in NiO content) with the increase in heat treatment temperature in the above temperature range in consistence with the XRD results (Fig. 1). Apart from the increase in Ni content, higher heat treatment temperature enhances the crystallinity and the particle size of the Ni/NiO composite structure collectively favoring the increase in magnetization.[93] This type of behavior is entirely consistent with the standard thermodynamic model of particle growth in a system in such a way that differences in the magnetic parameters are associated with changes in the particle size.[94] Canting ferromagnetism at the surface of tiny pristine NiO nanoparticles originating from the surface spin disorder in the AFM layer will get diminished with the increase in particle size.[95,96] However, in the present case, the NiO layer becomes thinner with the increase in the heat treatment temperature, ultimately favoring the canting ferromagnetism effect in the samples derived at higher temperatures. In all the samples, the magnetization shows a rapid increase at low fields, followed by a moderate non-linear increase and then a high field linear behavior. Similar type of behavior in the *M-H* curve of Ni/NiO nanoparticles were reported by Kar *et al*[6], and Roy *et al*.[33] As given in Table 1, the $M_S$ in the derived samples is much lower than that of bulk pristine Ni ($M_S$ = 55 emu/g),[2,93] which is essentially due to two primary reasons. First, magnetic nanoparticles are expected to exhibit reduced magnetization due to the large percentage of surface spins, with disordered magnetic orientation.[97] Second, in the present samples the surface interfacing with the AFM NiO layer and

the presence of the outer graphitic carbon layer are also significantly responsible for the decrease in $M_S$. Further reasons include electron exchange between core and surface atoms which may quench the moment.[17] The existence of the NiO layer rules out possible proximity effects between ferromagnetic Ni and carbon.[98] Such effects were proposed to explain ferromagnetism in carbon.[99,100] In contrast, the coercivity ($H_C$) values in all the samples are much higher compared to the reported $H_C$ in bulk Ni (~100 Oe),[100] which is primarily because of the typical Ni/NiO core/shell nanostructure.[101] The $H_C$ values gradually increased in the samples (a-c), and then decreased in the sample (d), derived at 600°C. While the increase in $M_S$ with the increase in particle size was primarily due to the increase in Ni core size and crystallinity, the observed variation in $H_C$ can be explained on the basis of domain structure, critical diameter, strains, magneto crystalline anisotropy and shape anisotropy of the crystals.[4,5,7] Interaction between the surface spins affect the surface anisotropy, leading to an increase in effective anisotropy.[102-104] Further contribution to the enhancement in $H_C$ is from the surface layer of graphitic carbon on the Ni/NiO core/shell nanostructure, which reorders the NiO surface spin to share a magnetic hardening of ideal Ni single domains of surface controlled shape anisotropy. Similar observations were reported by Singh *et al*[105] in carbon encapsulated nickel nanotubules. The squareness ratio, $S$ is a well known indicator of domain structure in FM materials and is defined as the ratio of $M_R$ and $M_S$, *i.e.,* $S = M_R/M_S$. If $S$ takes a value close to 0.5, it implies that the sample is having single magnetic domains.[8,30,106] As given in Table 1, the S-values gradually increased in the samples with the increase in heat treatment temperature, and reaches a value of 0.45 in the samples derived at 500°C. The $S$-value reduced to 0.39 (along with a reduction in the $H_C$) on further increasing the processing temperature to 600°C. The bit smaller $S$-value in comparison to an ideal single domain value of 0.5 in the randomly oriented single FM Ni domains (in the samples derived at 500°C) suggests that the FM core particles are interacting via an AFM NiO phase supported by the graphitic carbon layer on the surface. The surface layer of graphitic carbon is playing an important role in determining the resultant magnetic properties.

To obtain qualitative information on the superparamagnetic effects and the blocking temperature ($T_B$) of the graphitic carbon coated Ni/NiO core/shell nanoparticles, the zero-field-cooled (ZFC) and field-cooled (FC) magnetization of the samples were recorded. Fig. 9 shows the magnetization vs. temperature ($M$-$T$) behavior of the graphitic carbon coated Ni/NiO samples processed at (a) 500°C and (b) 600°C under ZFC and FC conditions from 80 K to 300 K at an

applied field of 500 Oe. The ZFC magnetization curves were obtained after the samples had been cooled to 80 K in absence of any external magnetic field from room temperature and then measured in presence of the field by increasing the temperature while the FC curves were obtained during cooling from room temperature in presence of the field.

As expected, both samples (Figs. 9a-b) exhibit irreversibility behavior, displaying hysteresis and remanence across the entire temperature range. The irreversibility behavior in the given temperature range confirms the existence of magnetically frustrated spin disorder system or clustered spin glassy system.[4,39,107,108] The shape of the ZFC branches of both samples are quite similar. The ZFC magnetization curves monotonically increases with increasing temperature while no significant change is observed in both FC curves as temperature decreases from 300 K to 80 K. During FC, as the temperature drops, the individual magnetic moments associated with each particle go from a totally disordered state, cancelling each other out over the entire specimen sample, to being aligned in a common direction (parallel to the field). For ZFC measurements, the magnetic nanoparticles were cooled to low temp with no applied field, ending up with low magnetization, since all the macrospins remain in random alignment. As we begin to heat up the sample, we approach the $T_B$, which is the temperature for which there is sufficient thermal energy to overcome the energy barrier between parallel and antiparallel alignment of the macrospin with respect to the anisotropy axis. So when the increasing temperature reaches the $T_B$, we see an abrupt but continuous increase of the magnetization. For an assortment of particle sizes (nanoparticles with uniaxial magnetic anisotropy - single domain "Stoner-Wohlfarth" particles), this abrupt change is smoothed out. So, as temperature increases, more and more particles go from blocked to superparamagnetic and are able to align with the small external applied field. As the temperature is further increased, the random fluctuations from thermal energy begin to dominate and the macrospins become randomly oriented once again, producing the 1/T exponential decrease of the magnetization that we see at higher temperatures. Superparamagnetic $T_B$ is generally associated with the maxima observed in ZFC curve.[109]

In the present samples, a complete irreversibility in the ZFC and FC curves can be seen right from the starting temperature of 300 K. This pertinent irreversibility in the ZFC/FC curves of Ni/NiO samples is indicative of some phase remaining blocked beyond the room temperature (300 K).[110] Thus, we conclude that the $T_B$ of the Ni cores of these bi-phase samples is above 300 K. Mathematically, $T_B$ can be defined as, $T_B = kV/25k_B$ for single domain particles (where, $k$ is

the magnetic anisotropy constant, $V$ the average volume of the ferromagnetic particles and $k_B$ the Boltzmann constant).[11] For Ni, $k = 5 \times 10^4$ erg/cm$^3$, which gives a value of 34 nm as the critical size of Ni nanoparticles to remain ferromagnetic at 300 K.[110,111] In the present case, the crystallite size of the Ni core is found to be 21 nm (samples derived at 500°C) and 31 nm (in samples derived at 600°C), which are shorter than the critical value and show an extended blocked regime above 300 K. The relatively flat nature of the FC curves indicates strong inter particle dipolar interactions which seem likely from the particle's close proximity to one another as evident from the SEM and TEM images.[7,35-37,112] Additionally, such behavior is possibly arising from the presence of superparamagnetic particles together with non-negligible fraction of nanoparticles still being in a blocked magnetic state at room temperature. This can happen due to several reasons such as broad size distribution, particle agglomeration or strong interparticle dipolar magnetic interactions.[109,113] The AFM NiO on the surface of the particles can be responsible for pinning the magnetization of the FM Ni core (also $E_B$ effect) and as a consequence the ZFC-FC plot can show non-overlapping behavior with competition between long range and short range order magnetization.[35-37,39,110] The coupling established at Ni and NiO interface provides a platform to enhance the magnetic stability of FM/AFM systems with increased $T_B$.

MR measurements were carried out on compact pellets of the derived Ni/NiO core/shell type nanoparticles. Fig. 10 shows the resistance change versus magnetic field measured at room temperature (290 K) of such a pellet comprising Ni/NiO nanoparticles derived at 600°C. The FM core/AFM shell type nanoparticles with an intrinsic coating of graphitic carbon show large negative MR, of the order of 10%. To the best of our knowledge, such a high value of MR at room temperature in Ni was not reported before. Pol *et al* [17] reported similar type of negative MR, of the order of 10% at 4 K in Ni nanospheres encapsulated in a fullerene like carbon. Bizyaev *et al*[20] reported anisotropic MR in Ni nanowires, typically of the order of 1%. Typical negative MR values of 0.2-0.5% at 5 K were reported by Bianco *et al*[21] in Ni nanocrystallites dispersed in NiO matrix.

A compact structure of the graphitic carbon coated Ni/NiO core/shell nanoparticles is analogous to an immobile ferro-fluid, which, in a simple way of saying, consists of tiny magnetic particles dispersed in an immobile liquid. In such structure, grain boundaries, separation between ferromagnetic particles or domains, and the intermediate phase (here, the shell structure of NiO

and the graphitic carbon) frame the basic parameters, which govern the magnetotransport properties according to size, morphology (renders shape anisotropy and in-turn affects the magnetic or MR properties) and orientation of the FM composite particles on the surrounding in a texture structure. The origin of MR in such specific examples is associated with the spin dependent tunneling of electrons between the FM particles through an insulating boundary or the surface barrier layer in an integral part of the FM particles of such a specific microstructure. In agreement with literature,[107,114-117] we conclude that in the present samples, the native surface layer of NiO and graphitic carbon in part of the Ni nanoparticles of a core-shell structure is acting as the tunneling barrier layer between such Ni nanoparticles in a hard compacted pellet. Possibly, the NiO and graphitic carbon interbridges the FM Ni particles in a specific conjugated electronic structure. When an external magnetic field is applied, it modulates the intergranular flow of spin-polarized Ni ($3d^9$) electrons tunneling over moderate field, leading to promoted MR properties.

The spin dependent tunneling, which is dominant at low temperatures, renders effectively an increasing value of MR over low temperatures. At high temperatures, a possible suppression of the MR value encounters mainly due to (i) the suppression of spin dependent contribution of the conductance and (ii) the increase of the spin independent conduction due to a higher order inelastic hopping of the electrons through the localized states in the self-confined barrier layer.[114-117] That is, besides the elastic process of the spin dependent intergranular tunneling, the imperfections in the grain boundary barriers support a possible hopping conductance channel.[116,117] Therefore, to maintain an effectively large MR value at high temperatures, one needs to control over the spin independent conduction by minimizing the imperfections in the grain boundaries, engineering the grain size, shape, orientation, and surface structure.

## Conclusions

Core/shell structured nanoparticles of Ni/NiO encapsulated in graphitic carbon were synthesized by a sol-gel type chemical method via a metal ion-polymer complex precursor. The core/shell structure in the derived samples can be customized by controlling the heat treatment temperature of the precursor powders. Structural analysis with XRD, XANES and EXAFS confirmed that the Ni content in the nanoparticles increases with the increase in heat treatment temperature with a gradual decay of the NiO phase. Both NiO and Ni phases in the particles have stable *fcc* crystal

structure with *Fm-3m* space group. Microstructural analysis with FESEM revealed marigold flower like morphology formed by loose clustering of the spherical Ni/NiO nanoparticles. HRTEM micrographs clearly revealed the core/shell structure in the nanoparticles. The magnetic properties of the derived samples can be conveniently tailored by tuning the particle microstructure for a wide range of pertinent applications. The $M_S$ values in the derived nanoparticles are in the range of 0.72-22.11 emu/g, much lower compared to bulk Ni value. This is primarily due to the nanosize effect along with the contributory effects from the secondary phases of AFM NiO and graphitic carbon. The $T_B$ of the FM Ni core in the derived samples is above 300 K, largely due to the exchange interaction at the interface between FM Ni and AFM NiO components. The surface functionalized Ni/NiO nanoparticles show a large negative MR at room temperature, *viz.*, -10% in the samples derived at 600°C. The *in situ* formation of the graphitic carbon layer on the Ni/NiO core/shell nanoparticles renders a specific conjugated electronic structure interbridging the FM Ni cores, which supports efficient spin dependent tunneling even at room temperature.

**Acknowledgments**

The authors sincerely express thanks to (i) S. C. S. College, Omerga, (ii) UGC-DAE Consortium for Scientific Research, Indore, (iii) North-Eastern Hill University, Shillong and (iv) S. N. Bose National Centre for Basic Sciences, Kolkata.

**References**

1. K. Sakiyama, K. Koga, T. Seto, M. Hirasawa and T. Orii, *J. Phys. Chem. B,* 2004, **108**, 523-529.
2. C. Parada and E. Moran, *Chem. Mater.,* 2006, **18**, 2719-2725.
3. S. Addato, V. Grillo, S. Altieri, R. Tondi, S. Valeri and S. Frabboni, *J. Phys. Condens. Matter,* 2011, **23**, 175003.
4. A. Kremenovic, B. Jancer, M. Ristic, M. Vucinic-Vasic, J. Rogan, A. Pacevski and B. Antic, *J. Phys. Chem. C,* 2012, **116**, 4356-4364.
5. F. Yuan, Y. Ni, L. Zhang, S. Yuan and J. Wei, *J. Mater. Chem. A,* 2013, **1**, 8438-8444.
6. N. Chopra, L. Claypoole and L. G. Bechas, *J. Nanopar. Res.,* 2010, **12**, 2883-2893.
7. C. Yuan, *J. Phys. Chem. C,* 2010, **114**, 2124-2126.
8. S. Kar and V. Singh, *J. Alloys Compd.,* 2011, **509**, 3582-3586.
9. B. Nayak, S. Vitta, A. Nigam and D. Bahadur, *Thin Solid Films,* 2006, **505**, 109-112.
10. M. Garza-Navarro, A. Torres-Castro, U. Ortiz and E. Rosa, *J. Solid State Chem.,* 2010, **183**, 99-104.
11. A. Johnston-Peck, J. Wang and J. Tracy, *ACS Nano,* 2009, **3**, 1077-1084.

12. C. Levin, C. Hoffman, T. Ali, A. Kelly, E. Morosan, P. Nordlander, K. Whitmire and N. Halas, *ACS Nano,* 2009, **3**, 1379-1388.
13. I. S. Lee, N. Lee, J. Park, B. H. Kim, Y. W. Yi, T. Kim, T. K. Kim, I. H. Lee, S. R. Paik and T. Hyeon, *J. Am. Chem. Soc.,* 2006, **128**, 10658-10659.
14. T. Seto, H. Akinaga, F. Takano, K. Koga, T. Orrie and M. Hirasawa, *J. Phys. Chem. B,* 2005, **109**, 13403-13405.
15. R. Evans, R. Yanes, O. Mryasov, R. Chantrell and O. Chubykalo-Fesenko, *Europhys. Lett.,* 2009, **88**, 57004.
16. R. Evans, D. Bate, R. Chantrell, R. Yanes and O. Chubykalo-Fesenko, *Phys. Rev. B,* 2011, **84**, 092404.
17. S. V. Pol, V. G. Pol, A. Frydman, G. N. Churilov and A. Gedanken, *J. Phys. Chem. B,* 2005, **109**, 9495-9498.
18. Y. Tomoda, S. Kayashima, T. Ogino, M. Motoyama, Y. Takemura and J. Shirakashi, *J. Magn. Magn. Mater.,* 2007**, 310**, e641-e643.
19. L. Bianco, F. Spizzo, M. Tamisari and A. Castiglioni, *J. Appl. Phys.,* 2011, **110**, 043922.
20. D. A. Bizyaev, A. A. Bukharaev, D. V. Lebedev, N. I. Nurgazizov and T. F. Khanipov, *Tech. Phys. Lett.,* 2012, **38**, 645.
21. L. Bianco, F. Spizzo, M. Tamisari and P. Allia, *J. Magn. Magn. Mater.,* 2013, **339**, 94-99.
22. J. McCloy, W. Jiang, T. Droubay, T. Varga, L. Kovarik, J. Sundararajan, M. Kaur, Y. Qiang, E. Burks and K. Liu, *J. Appl. Phys.,* 2013, **114**, 083903.
23. Z. P. Huang, D. Z. Wang, J. G. Wen, M. Sennett, H. Gibson and Z. F. Ren, *Appl. Phys. A,* 2002**, 74**, 387-391.
24. Y. F. Guan, R. C. Pearce, A. V. Melechko, D. K. Hensley, M. L. Simson and P. D. Rack, *Nanotechnology,* 2008, **19**, 235604.
25. J. Park, E. Kang, S. Son, H. Park, M. Lee, J. Kim, K. Kim, H.-J. Noh, J.-H. Park, C. Bae, J.-G. Park and T. Hyoen, *Adv. Mater.,* 2005, **17**, 429-434.
26. J. M. Caruge, J. E. Helpert, V. Bulovic and M. G. Bawendi, *Nano Lett.,* 2006, **6**, 2991-2994.
27. X. Li, A. Dhanabalan and C. Wang, *J. Power Sources,* 2011, **196**, 9625-9630.
28. W. Wen, J.-M. Wu and M.-H. Cao, *J. Mater. Chem. A,* 2013, **1**, 3881-3885.
29. X. Yan, X. Tong, J. Wang, C. Gong, M. Zhang and L. Liang, *Mater. Lett.,* 2013, **106**, 250-253.
30. V. Singh and V. Srinivas, *Phys. Rev. B,* 2010, **82**, 054417.
31. O. Palchik, S. Avivi, D. Pinkert and A. Gedanken, *Nanostruct. Mater.,* 1999, **11**, 415-420.
32. X. Liu, U. Meridor, P. Zhao, G. Song, A. Frydman and A. Gedanken, *J. Magn. Magn. Mater.,* 2006, **301**, 13-21.
33. A. Roy, V. Srinivas, S. Ram, A. De Toro and J. Riveiro, *J. Appl. Phys*., 2004, **96**, 6782-6788.
34. K.M. Rahulan, N. Padmanathan, R. Philip, S. Balamurugan and C.C. Kanakam, *Appl. Surf. Sci.,* 2013, **282**, 656-661.
35. L. Bianco, F. Boscherini, A. Fiorini, M. Tamisari, F. Spizzo, M. Antisari and E. Piscopiello, *Phys. Rev. B,* 2008, **77**, 094408.
36. S. Guo, W. Liu, H. Meng, X. H. Liu, W. J. Gong, Z. Han and Z. D. Zhang, *J. Alloys Compd.,* 2010, **497**, 10-13.

37. F. Feygenson, A. Kou, L. E. Kreno, A. L. Tiano, J. M. Patete, F. Zhang, M. S. Kim, V. Solovyov, S. S. Wong and M. C. Aronson, *Phys. Rev. B,* 2010, **81**, 014420.
38. W. L. Jang, Y. M. Lu, C. L. Dong, W. S. Hwang, P. H. Hsieh, C. L. Chen and T. S. Chan, *Sci. Adv. Mater.,* 2013, **5**, 1346-1353.
39. M. K Singh, A. Agarwal, R.K. Swarnakar, R. Gopal and R. K. Kotnala, *Sci. Adv. Mater.,* 2012, **4**, 532-536.
40. M. Jamal, M. Hasan, M. Schmidt, N. Petkov, A. Mathewson and K. Razeeb, *J. Electrochem. Soc.,* 2013, **160**, B207-B212.
41. M. Thakur, M. Patra, S. Mujumdar and S. Giri, *J. Alloys Compd.,* 2009, **480**, 193-197.
42. F. A. Harraz, R. M. Mohamed, A. Shawky and I. A. Ibrahim, *J. Alloys Compd.,* 2010, **508**, 133-140.
43. M. Karimipour, J. M. Wikberg, V. Kapaklis, N. Shahtahmasebi, M. R. R. Abad, M. Yeganeh, M. M. Bagheri-Mohagheghi and P. Svedlindh, *Phys. Scr.,* 2011, **84**, 035702.
44. D. Bhattacharyya, A. K. Poswal, S.N. Jha, Sangeeta and S. C. Sabharwal, *Nucl. Instrum. Methods Phys. Res. Sect. A,* 2009, **609**, 286-293.
45. A. Gaur, B. D. Shrivastava, D. C. Gaur, J. Prasad, K. Srivastava, S. N. Jha, D. Bhattacharyya, A. Poswal and S. K. Deb, *J. Coord. Chem.,* 2011, **64**, 1265-1275.
46. S. Biswas and S. Ram, *Chem. Phys.,* 2004, **306**, 163-169.
47. S. Biswas, V. Srivastava and S. Ram, *J. Phys. Chem. C,* 2007, **111**, 7593-7598.
48. V. Perebeinos, S. W. Chan and F. Zhang, *Solid State Commun.,* 2002, **123**, 295-297.
49. M. A. Peck and M. A. Langell, *Chem. Mater.,* 2012, **24**, 4483-4490.
50. V. Singh, B. R. Mehta, S. K. Sengar, P. K. Kulriya, S. A. Khan and S. M. Shivaprasad, *J. Phys. Chem. C,* 2015, **119**, 14455-14460.
51. H. S. Nalwa, *Handbook of Nanostructured Materials and Nanotechnology,* Academic Press: San Diego, CA, 1994, 179.
52. S. Rana, S. Ram, S. Seal and S. K. Roy, *Appl. Surf. Sci.,* 2004, **236**, 141-154.
53. I. G. Morozov, O. Belousova, M. V. Kuznetsov, D. Ortega and I. P. Parkin, *J. Mater. Chem.,* 2012, **22**, 11214-11223.
54. D. Ortega, M. V. Kuznetsov, Y. G. Morozov, O. V. Belousova and I. P. Parkin, *J. Alloys Compd.,* 2013, **579**, 495-501.
55. Y. K. Chen-Wiegart, W. M. Harris, J. J. Lombardo, W. K. S. Chiu and J. Wang, *Appl. Phys. Lett.,* 2012, **101**, 253901.
56. D. Pan, J. K. Jian, A. Ablat, J. Li and Y. F. Sun, *Appl. Phys. Lett.,* 2012, **112**, 053911.
57. J. Yuh and W. M. Sigmund, *Ceram. Process. Res.,* 2015, **16**, 93-97.
58. D. C. Koningsberger and R. Prins, *X-ray Absorption: Principles, Applications, Techniques of EXAFS, SEXAFS and XANES;* John Wiley & Sons: New York, 1988, 321.
59. M. Newville, B. Ravel, D. Haskel, J. Rehr, E. A. Stern and Y. Yacoby, *Physica B,* 1995, **208 & 209**, 154-156.
60. Y. Zhou, J. Chen, B. Tay, J. Hu, G. Chow, T. Liu and P. Yang, *Appl. Phys. Lett.,* 2007, **90**, 043111.
61. P. Migowski, G. Machado, S. Texeira, M. Alves, J. Morais, A. Traverse and J. Dupanto, *Phys. Chem. Chem. Phys.,* 2007, **9**, 4814-4821.
62. A. Anspoks and A. Kuzmin, *Non-Cryst. Solids,* 2011, **357**, 2604-2610.
63. S. Qiu, Z. Zhou, J. Dong and G. Chen, *J. Tribol.,* 2001, **123**, 441-443.
64. J. Paredes, S. Villar-Rodil, A. Martinez-Alonso and J. Tascon, *Langmuir,* 2008, **24**, 10560–10564.

65. Y. Zhu, S. Murali, W. Cai, X. Li, J. Suk, J. Potts and R. Ruoff, *Adv. Mater.,* 2010, **22**, 3906-3924.
66. Q. Zhang, C. Tian, A. Wu, T. Tan, L. Sun, L. Wang and H. Fu, *J. Mater. Chem.,* 2012, **22**, 11778-11784.
67. A. Ferrari, *Solid State Commun.,* 2007, **143**, 47-57.
68. K.N. Kudin, B. Ozbas, H.C. Schniepp, R.K. Prud'homme, I.A. Aksay and R. Car, *Nano Lett.,* 2008, **8**, 36-41.
69. N.R. Wilson, P.A. Pandey, R. Beanland, R.J. Young, I.A. Kinloch, L. Gong, Z. Liu, K. Suenaga, J.P. Rourke, S.J. York and J. Sloan, *ACS Nano,* 2009, **3**, 2547-2556.
70. H. Kang, A. Kulkarni, S. Stankovich, R.S. Ruoff and S. Baik, *Carbon,* 2009, **47**, 1520-1525.
71. A. Ferrari, J. C. Meyer, V. Scardaci, C. Casiraghi, M. Lazzeri, F. Mauri, S. Piscanec, D. Jiang, K. Novoselov and S. Roth, *Phys. Rev. Lett.,* 2006, **97**, 187401.
72. Z. Luo, T. Yu, Z. Ni, S. Lim, H. Hu, J. Shang, L. Liu, Z. Shen, J. Lin, *J. Phys. Chem. C,* 2011, **115**, 1422-1427.
73. G. Zhou, D.-W. Wang, L.-C. Yin, N. Li, F. Li and H.-M. Cheng, *ACS Nano,* 2012, **6**, 3214-3223.
74. Y. Liu, C. Pan and J. Wang, *J. Mater. Sci.,* 2004, **39**, 1091–1094.
75. G. Malgas, C. Arendse, N. Cele and F. Cummings, *J. Mater. Sci.,* 2008, **43**, 1020–1025.
76. H. Wu, G. Wu, Q. Wu and L. Wang, *Mater. Charact.,* 2014, **97**, 18-26.
77. K. G. Chandrappa, T. V. Venkatesha, K. O. Nayana and M. K. Punithkumar, *Mater. Corros.,* 2011, **63**, 445−455.
78. J. J. Liu, W. Lv, W. Wei, C. Zhang, Z. J. Li, B. H. Li, F. Y. Kang and Q. H. Yang, *J. Mater. Chem. A,* 2014, **2**, 3031-3037.
79. Z. S. Wu, W. C. Ren, L. Wen, L. B. Gao, J. P. Zhao, Z. P. Chen, G. M. Zhou, F. Li and H. M. Cheng, *ACS Nano,* 2010, **4**, 3187–3194.
80. C. Wu, H. Zhang, Y. X. Wu, Q. C. Zhuang, L. L. Tian and X. X. Zhang, *Electrochimica Acta,* 2014, **134**, 18-27.
81. Y. Wang, S. Zhang, D. Du, Y. Shao, Z. Li, J. Wang, M. H. Engelhard, J. Li and Y. Lin, *J. Mater. Chem.,* 2011, **21**, 5319-5325.
82. V. Sridhar, I. Lee, H. H. Chun and H. Park, *RSC Adv.,* 2015, **5**, 68270-68275.
83. H. Estrade-Szwarckopf, *Carbon*, 2004, **42**, 1713-1721.
84. G. Bepete, D. Voiry, M. Chhowalla, Z. Chiguvare and N. J. Coville, *Nanoscale,* 2013, **5**, 6552–6557.
85. H. Yu, Y. Jin, F. Peng, H. J. Wang and J. Yang, *J. Phys. Chem. C,* 2008, **112**, 6758-6763.
86. K. L. Ma, J. X. Tang, Y. S. Zou, Q. Ye, W. J. Zhang and S. T. Lee, *Appl. Phys. Lett.,* 2007, **90**, 092105.
87. M. Hassan, E. Haque, K. R. Reddy, A, I. Minett, J. Chen and V. J. Gomes, *Nanoscale*, 2014, **20**, 11988-11994.
88. T. N. Narayanan, Z. Liu, P. R. Lakshmy, W. Gao, Y. Nagaoka, D. Sakhti Kumar, J. Lou, R. Vajtai and P. M. Ajayan, *Carbon,* 2012, **50**, 1338-1345.
89. S. Moussa, A. R. Siamaski, B. F. Gupton and M. S. El-Shall, *ACS Catal.,* 2012, **2**, 145–154.
90. J. F. Moulder, W. F. Stickle, P. E. Sobol and K. D. Bomben, *Handbook of X-ray Photoelectron Spectroscopy;* Perkin-Elmer Corporation: Eden Prairie, MN; 1992.

91. Y. Jeon, D. H. Park, J. I. Park, S. H. Yoon, I. Mochida, J. H. Choy and Y. G. Shul, *Sci. Rep.,* 2013, **3**, 2902.
92. L. Qiao and X. Bi, *Europhys. Lett.,* 2011, **93**, 57002.
93. Z. Li, Y. Su, Y. Liu, J. Wang, H. Geng, P. Sharma and Y. Zhang, *CrystEngComm.,* 2014, **16**, 8442-8448.
94. N. D. S. Mohallem and L. M. Seara, *Appl. Surf. Sci.,* 2003, **214**, 143-150.
95. J. M. Wesselinova, *J. Magn. Magn. Mater,* 2010, **322**, 234-237.
96. D. Li, Z. Han, J. G. Zheng, X. L. Wang, D. Y. Geng, J. Li and Z. D. Zhang, *J. Appl. Phys.,* 2009, **106**, 053913.
97. R. H. Kodama, A. E. Berkowitz, E. J. McNiff and S. Foner, *Phys. Rev. Lett.,* 1996, **77**, 394.
98. R. Hohne, M. Ziese and P. Esquinazi, *Carbon,* 2004, **42**, 3109-3114.
99. J. M. D. Coey, M. Venkatesan, C. B. Fitzgerald, A. P. Douvalis and I. S. Sanders, *Nature,* 2002, **420**, 156-159.
100. X. M. Ni, Q. B. Zhao, D. E. Zhang, X. J. Zhang and H. G. Zheng, *J. Phys. Chem. C,* 2007, **111**, 601-605.
101. A. B. Nawale, N. S. Kanhe, K. R. Patil, S. V. Bhoraskar, V. L. Mathe and A. K. Das, *J. Alloys Compd.,* 2011, **509**, 4404-4413.
102. S. Laureti, G. Varvaro, A. M. Testa, D. Fiorani, E. Agostinelli, G. Piccaluga, A. Musinu, A. Ardu and D. Peddis, *Nanotechnology,* 2010, **21**, 315701.
103. V. Blanco-Gutierrez, M. Virumbrales, R. Saez-Puche and M. J. Torralvo-Fernandez, *J. Phys. Chem. C,* 2013, **117**, 20927-20935.
104. S. T. Xu, Y. Q. Ma, G. H. Zheng and Z. X. Dai, *Nanoscale,* 2015, **7**, 6520-6526.
105. V. Singh, S. Ram, M. Ranot, J. G. Park and V. Srinivas, *Appl. Phys. Lett.,* 2008, **92**, 253104.
106. M. Maisnam, S. Phanjoubam, H. N. K. Sarma, L. R. Devi, O. P. Thakur and C. Prakash, *Physica B,* 2004, **352**, 86-90.
107. D. Peddis, C. Cannas, A. Musinu and G. Piccaluga, *Chem. Eur. J.,* 2009, **15**, 7822-7829.
108. Z. M. Tian, S. Huang, Y. Qiu, S. L. Yuan, Y.Y. Wu and L. Li, *J. Appl. Phys.,* 2013, **113**, 143906.
109. A. Roy, J. A. De Toro, V. S. Amaral, P. Muniz, J. M. Riveiro and J. M. F. Ferreira, *J. Appl. Phys.,* 2014, **115**, 073904.
110. J. Nogues, V. Langlais, J. Sort, S. Doppiu, S. Surinach and M. D. Baro, *J. Nanosci. Nanotechnol.,* 2008, **8**, 2923-2928.
111. K. P. Donegan, J. F. Godsell, J. M. Tobin, J. P. O'Byrne, D. J. Otway, M. A. Morris, S. Roy and J. D. Holmes, *CrystEngComm*, 2011, **13**, 2023-2028.
112. S. Banerjee, S. Roy, J. W. Chen and D. Chakravorty, *J. Magn. Magn. Mater.,* 2000, **219**, 45-52.
113. J. Tang, L. Feng and J. A. Wiemann, *Appl. Phys. Lett.,*1999, **74**, 2522-2524.
114. J. Dai and J. Tang, *Appl. Phys. Lett.,* 2000, **77**, 2840-2842.
115. X. Zhang, Y. Chen and Z. Li, *J. Magn. Magn. Mater.,* 2006, **307**, 134–138.
116. N. V. Dalakova, B. I. Belevtsev, E. Y. Beliayev, A. N. Bludov and V. N. Pashchenko, *Low Temp. Phys.,* 2012, **38**, 1121-1128.
117. S. Biswas, G. P. Singh, S. Ram and H.-J. Fecht, *J. Magn. Magn. Mater.*, 2013, **339**, 175-181.

## Figure captions

**Fig. 1.** X-ray diffraction in the derived graphitic carbon coated Ni/NiO core/shell nanoparticles after a heat treatment of the $Ni^{2+}$-PVA-sucrose polymer precursor powders at (a) 400°C, (b) 450°C, (c) 500°C, and (d) 600°C, respectively for 2 h in ambient air.

**Fig. 2.** (a) Normalized XANES spectra of the derived graphitic carbon coated Ni/NiO samples along with Ni and NiO standards. Experimental XANES data (scatter points) and linear combination fitting curves (solid line) for the samples treated at (b) 500°C and (c) 600°C along with their standards.

**Fig. 3.** EXAFS signal $\chi(k)$ weighted by $k$ from the derived graphitic carbon coated Ni/NiO samples along with Ni and NiO standards. (b) Fourier transformed EXAFS spectra of the samples along with Ni and NiO standards at Ni K-edge (scatter points) and the theoretical fits (solid lines). The individual curves are vertically shifted by 0.3 $Å^{-2}$.

**Fig. 4.** FESEM images of graphitic carbon coated Ni/NiO core/shell nanoparticles derived after a heat treatment of the precursor powders at (a) 500°C and (b) 600°C for 2 h in ambient air. (c) EDX spectrum of the Ni/NiO nanoparticles obtained at 500°C.

**Fig. 5.** HRTEM images of graphitic carbon coated Ni/NiO core/shell nanoparticles obtained after a heat treatment of the precursor powders at (a) 400°C and (b) 500°C for 2 h in ambient air. The magnified image in the inset shows the finer details of the core/shell architecture. (c) Further magnification reveals the crystalline planes in the highly dispersed particles (derived at 500°C). (d) SAED pattern of the samples treated at 500°C.

**Fig. 6.** Raman spectra of the derived graphitic carbon coated Ni/NiO core/shell nanoparticles after heating the $Ni^{2+}$-PVA-sucrose polymer precursor powders at (i) 400°C, (ii) 500°C, and (iii) 600°C for 2 h in ambient air. The peaks corresponding to the graphitic structure induced G-band and the defect induced D-band appear in the vicinities of 1590 $cm^{-1}$ and 1350 $cm^{-1}$, respectively.

**Fig. 7.** (a) XPS spectrum of graphitic carbon coated Ni/NiO core/shell nanoparticles derived at 400°C. Deconvoluted spectra showing the splitting of (b) 1s O-band and (c) 1s C-band with finer details. The deconvoluted spectrum (b) reveals a triplet O1s band in $O^{2-}$ bridging to C-atoms of a distinct surface layer and $O^{2-}$ of NiO. The surface interface shares the prominent band. Similarly, after deconvolution, the XPS spectrum (d) reveals the details of $3p_{3/2}$ Ni-band. (e) A schematic representation of the graphitic carbon coated Ni/NiO core/shell nanostructure.

**Fig. 8.** Room temperature magnetic hysteresis curves (*M-H*) of graphitic carbon coated Ni/NiO core/shell nanoparticles derived after a heat treatment of the precursor powders at (a) 400°C, (b) 450°C, (c) 500°C, and (d) 600°C for 2 h in ambient air.

**Fig. 9.** Low temperature magnetic hysteresis (*M-T*) curves of graphitic carbon coated Ni/NiO core/shell nanoparticles derived after a heat treatment of the precursor powders at (a) 500°C and (b) 600°C for 2 h in ambient air.

**Fig. 10.** Room temperature magnetoresistance in a compact pellet of Ni/NiO core/shell nanoparticles derived at 600°C. The inset figure shows a model conjugated electronic structure interbridging the FM Ni cores, which supports efficient spin dependent tunneling.

## Table captions

**Table 1: Structural and magnetic properties of the derived Ni/NiO core/shell nanoparticles.**

**Table 2: Structural parameters of the derived Ni/NiO nanoparticles obtained from EXAFS analysis.**

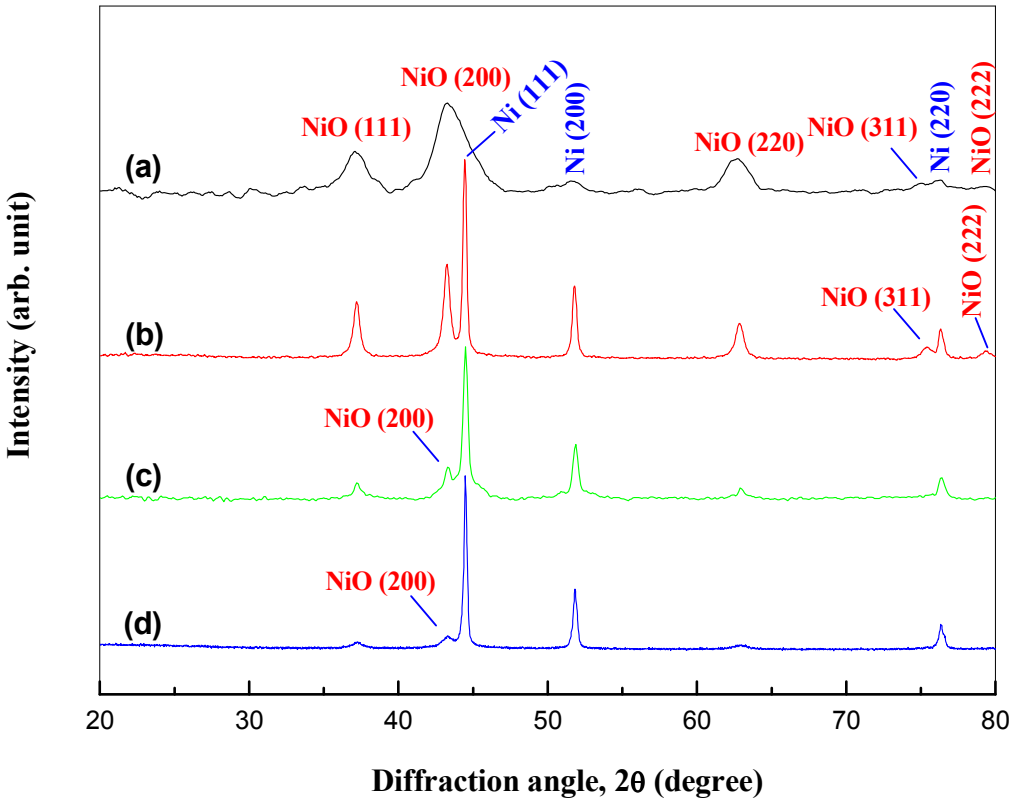


**Figure 1.**

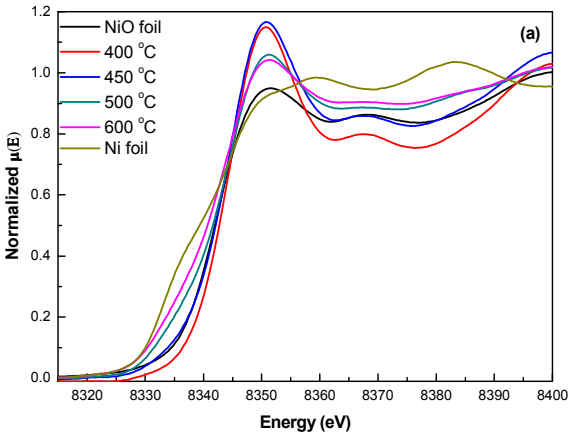

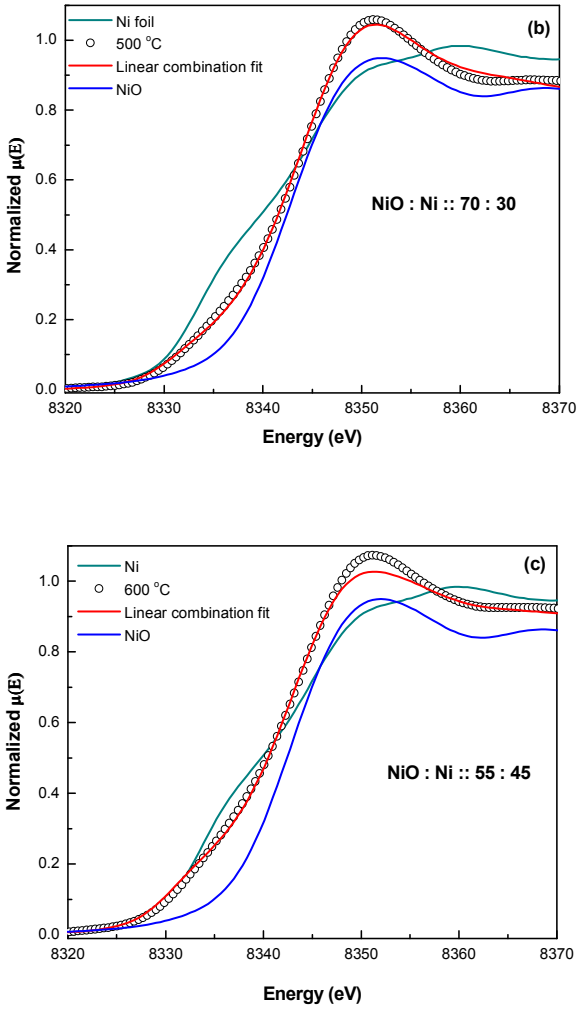


**Figure 2.**

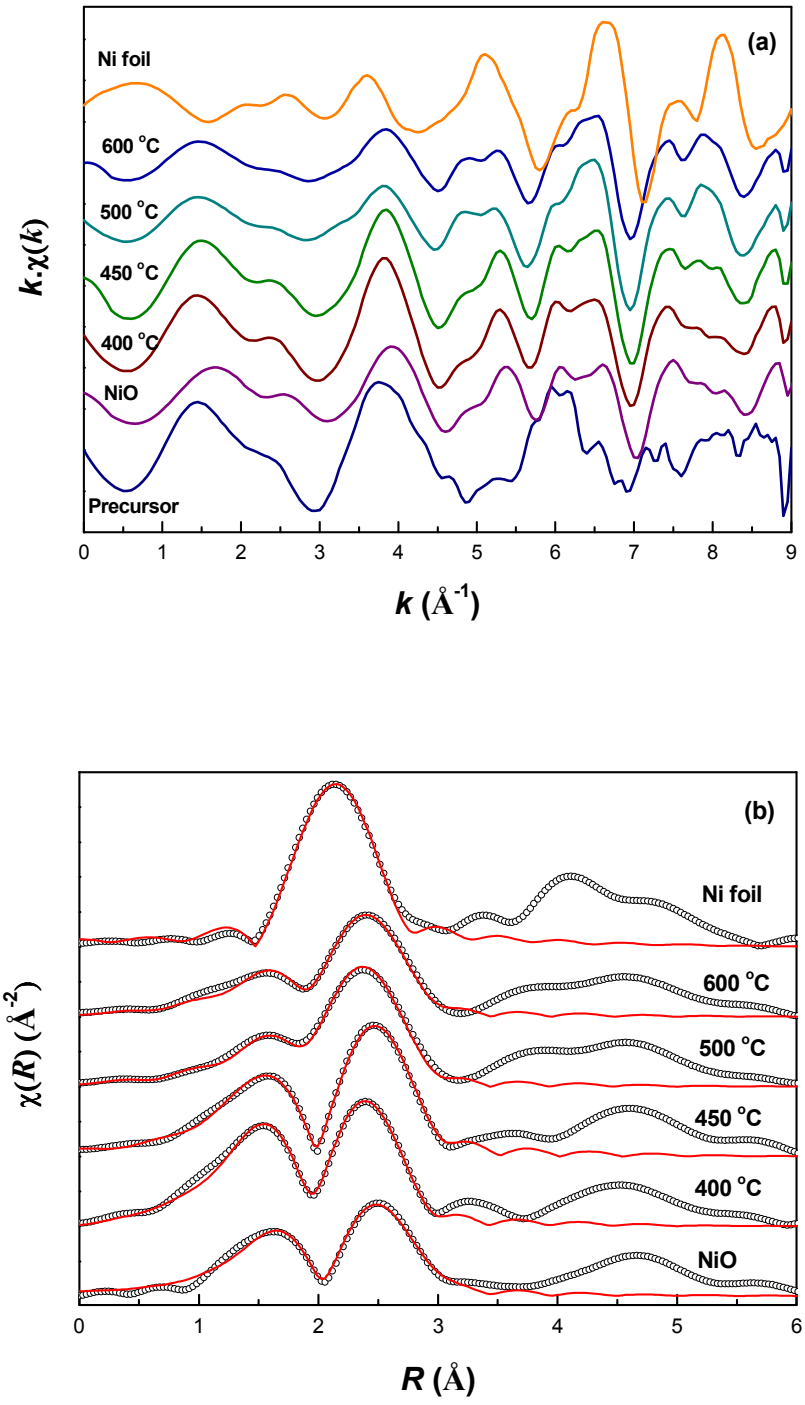


**Figure 3.**

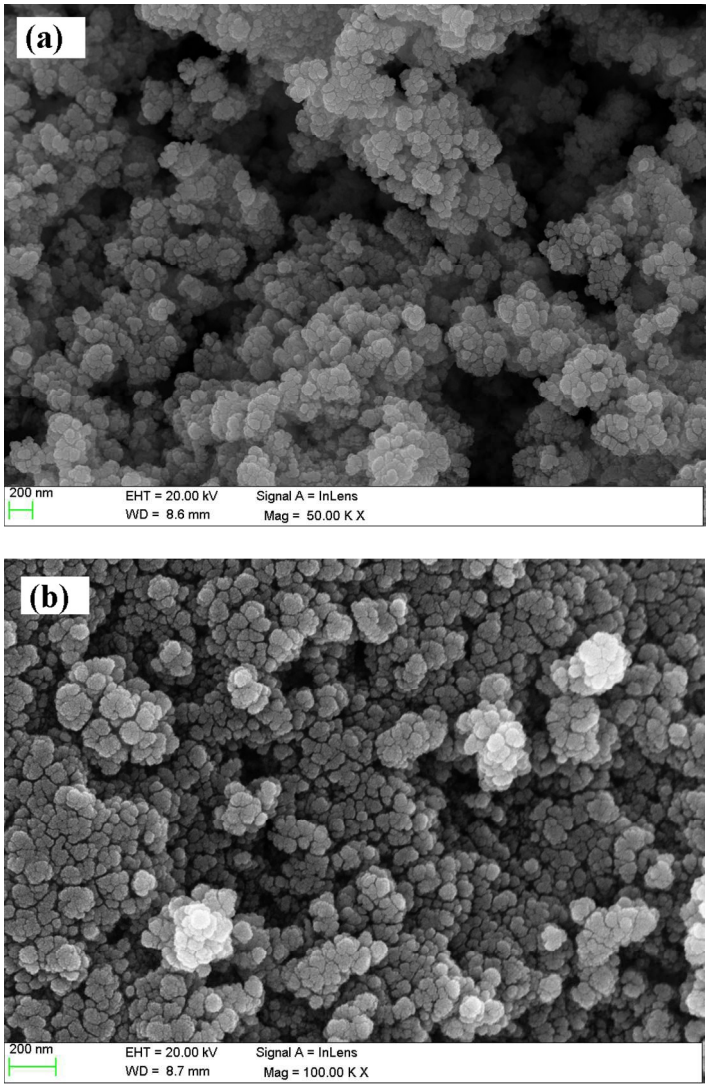


**Figure 4.**

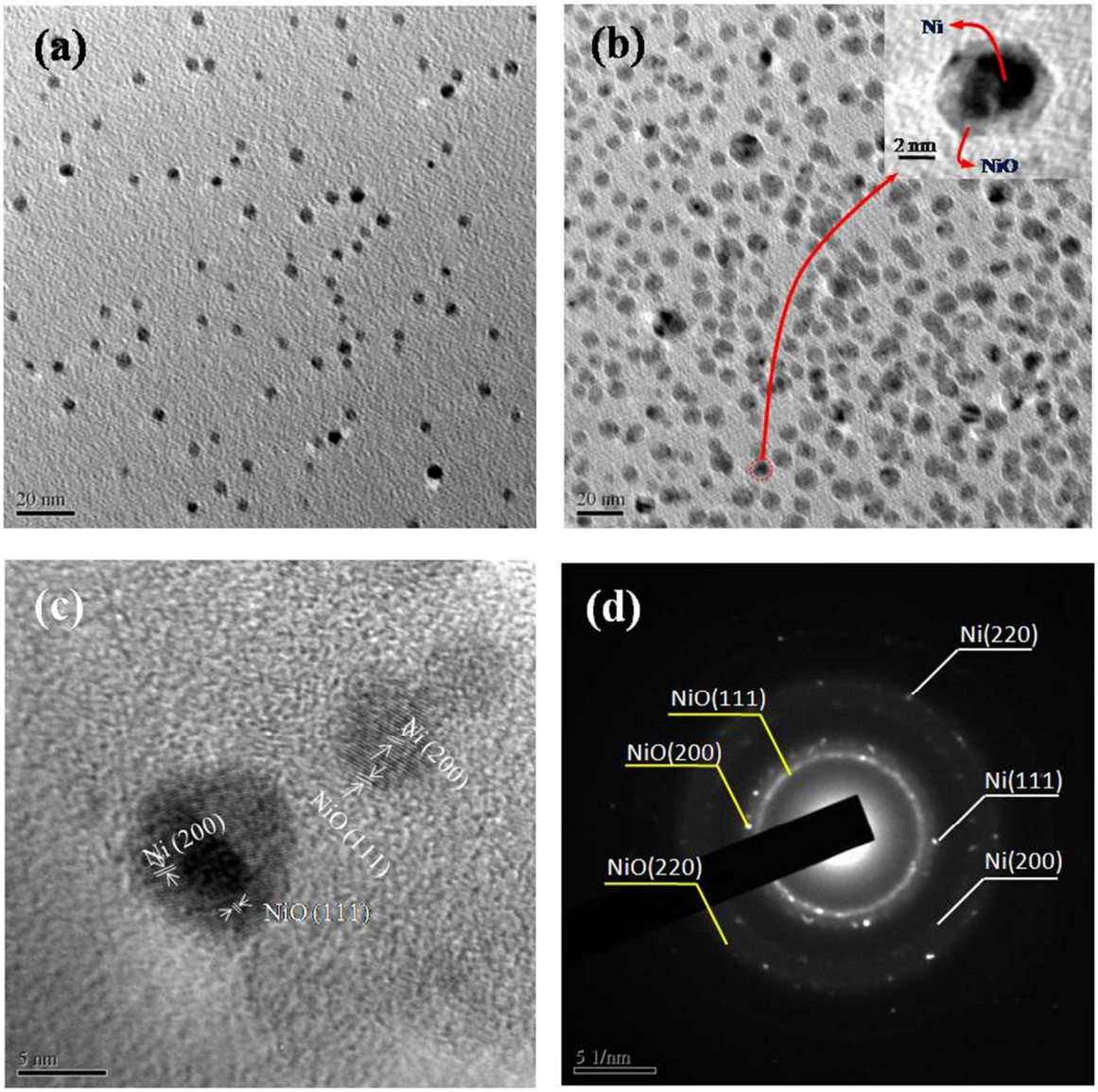


**Figure 5.**

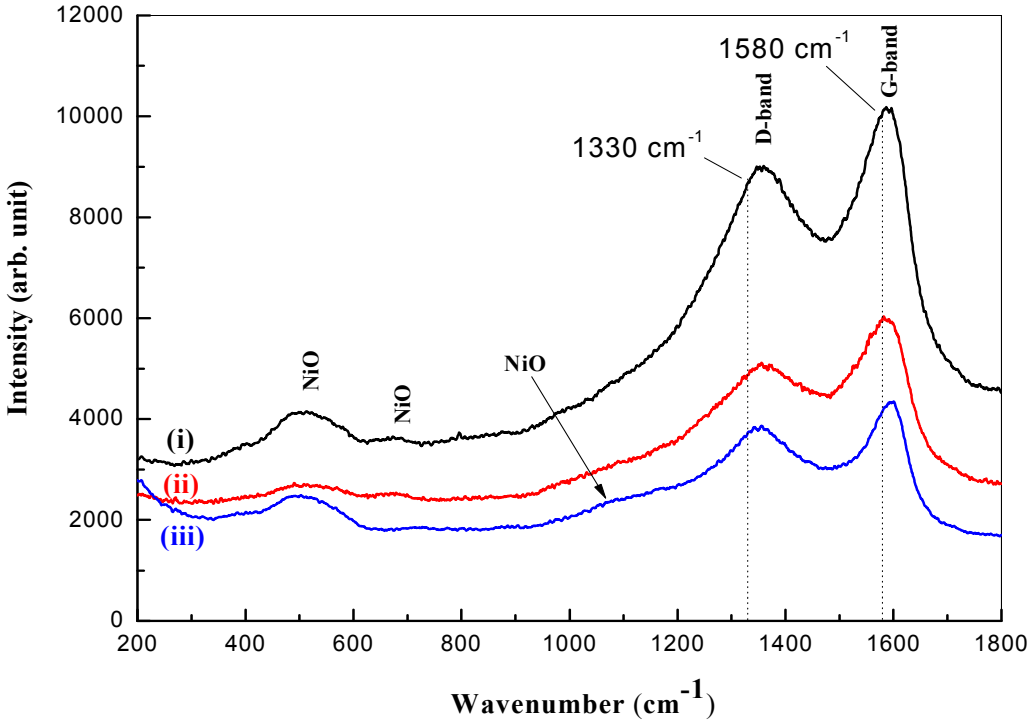


**Figure 6.**

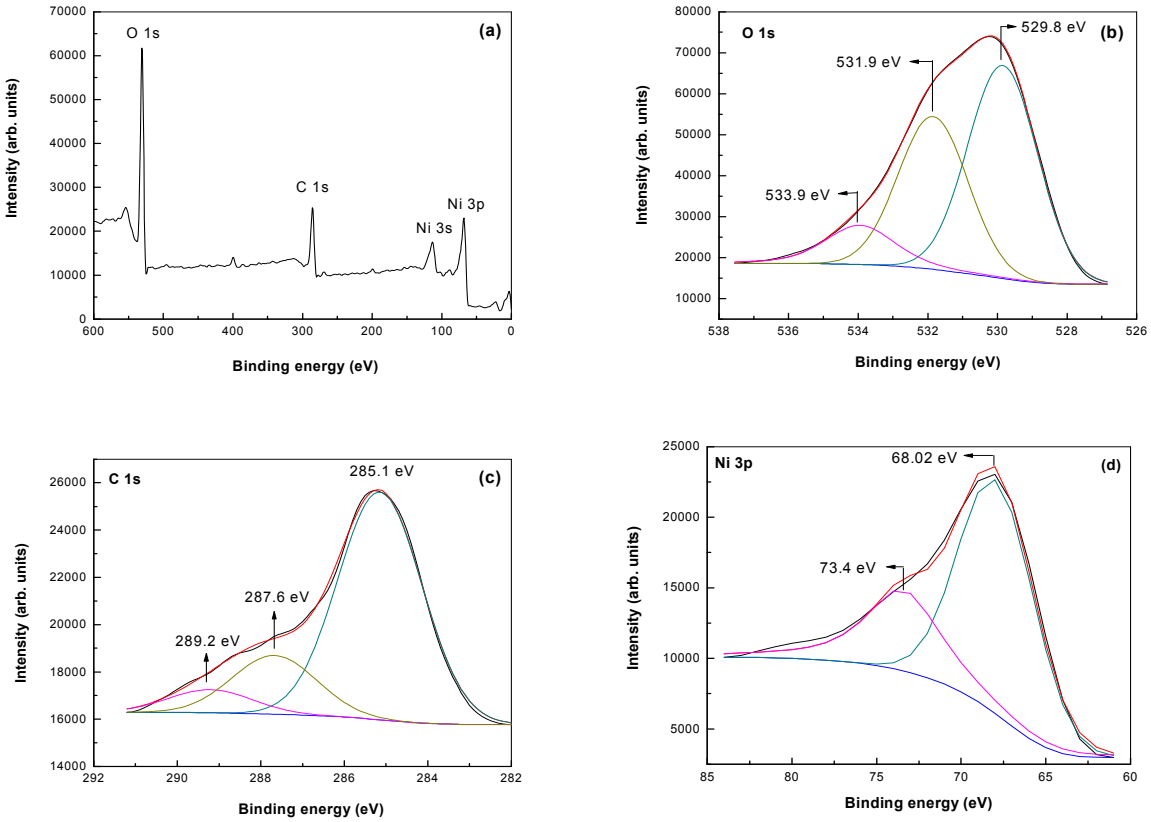


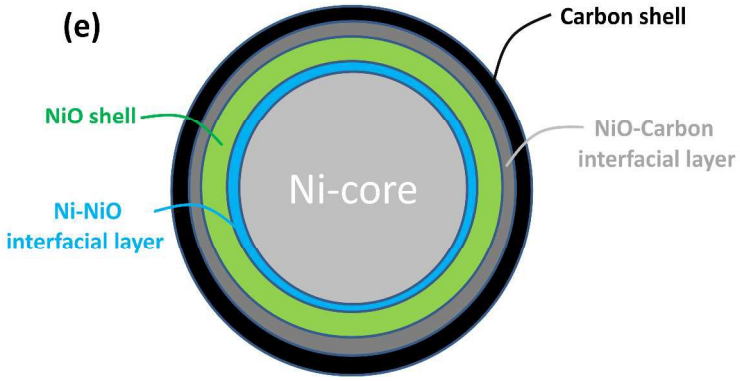


**Figure 7.**

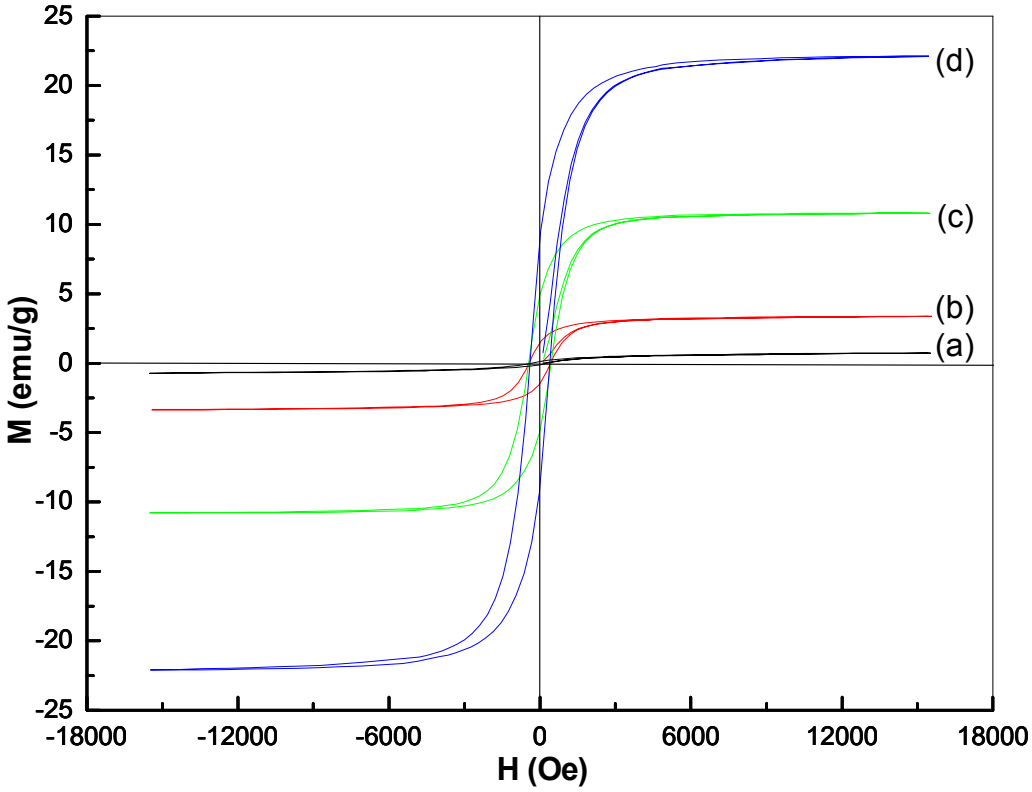


**Figure 8.**

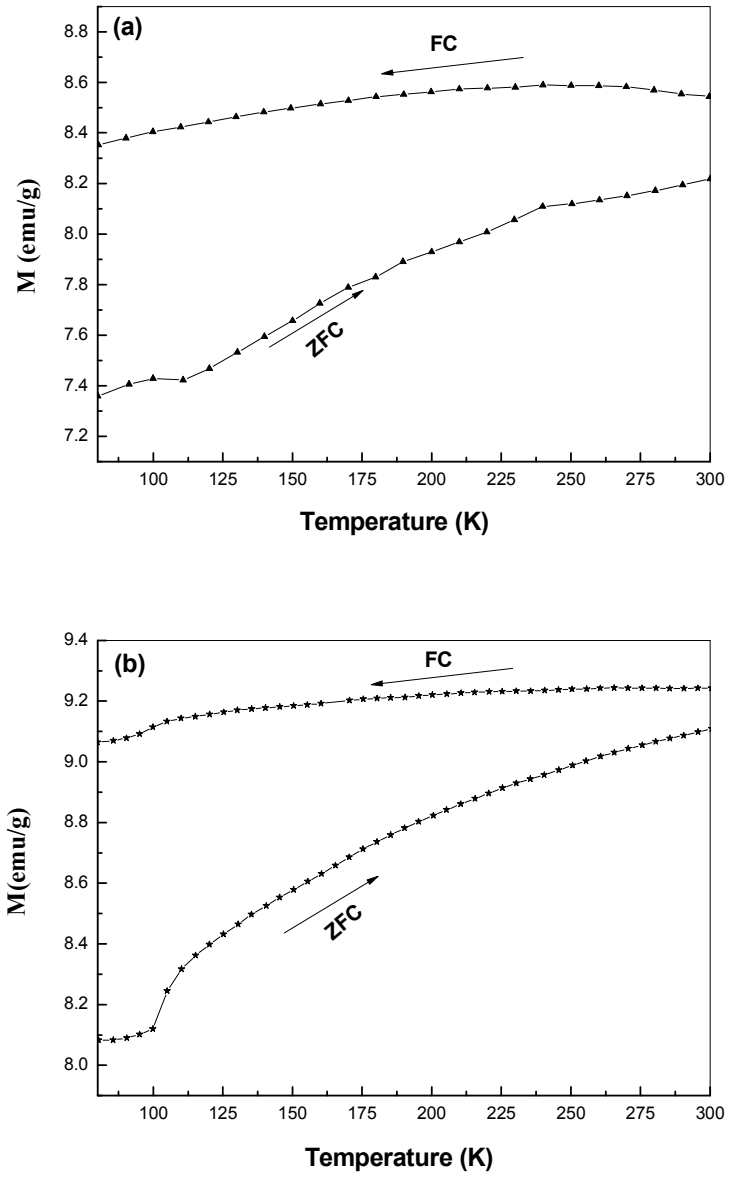


**Figure 9.**

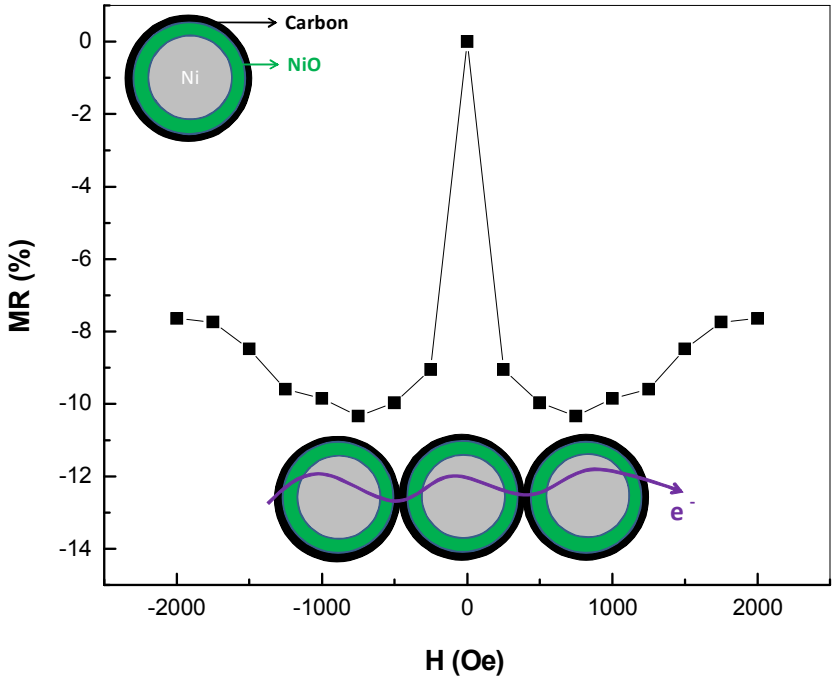


**Figure 10.**

**Table 1.**

| Final composition (heat treatment temp.) | Lattice constant $a$ (nm) | | Lattice volume $V_0$ (x $10^{-3}$ $nm^3$) | | Density $\rho$ (g/cc) | | Average crystallite size $d$ (nm) | | $V_{XRD}$ (at.%) | | Magnetic properties | | | | References |
|---|---|---|---|---|---|---|---|---|---|---|---|---|---|---|---|
| | NiO | Ni | NiO | Ni | NiO | Ni | NiO | Ni | NiO | Ni | $M_S$ (emu/g) | $M_R$ (emu/g) | $H_C$ (Oe) | $S$ | |
| **Ni/NiO (400°C)** | 0.4196 | 0.3540 | 73.87 | 44.66 | 6.7186 | 8.7929 | 5 | 4 | 91.2 | 8.8 | 0.72 | 0.12 | 340.12 | 0.16 | Present work |
| **Ni/NiO (450°C)** | 0.4198 | 0.3543 | 73.98 | 44.47 | 6.7090 | 8.6799 | 11 | 19 | 81 | 19 | 3.37 | 1.47 | 428.77 | 0.43 | Present work |
| **Ni/NiO (500°C)** | 0.4190 | 0.3540 | 73.56 | 44.66 | 6.7475 | 8.7929 | 16 | 21 | 63.3 | 36.7 | 10.79 | 4.86 | 441.86 | 0.45 | Present work |
| **Ni/NiO (600°C)** | 0.4192 | 0.3538 | 73.66 | 44.28 | 6.7379 | 8.8069 | 18 | 31 | 52.8 | 47.2 | 22.11 | 8.71 | 394.88 | 0.39 | Present work |
| **Bulk NiO** | 0.4177 | - | 72.87 | - | 6.8109 | - | - | - | - | - | - | - | - | - | JCPDS(card 89-7130) |
| **Bulk Ni** | - | 0.3523 | - | 43.76 | - | 8.9110 | - | - | - | - | 55 | 2.7 | 100 | - | JCPDS (card 87-0712), [2], [93], [100] |

**Table 2.**

| Paths | Parameters | Bulk values** | Samples derived after heat treating at | | | |
|---|---|---|---|---|---|---|
| | | | 400°C | 450°C | 500°C | 600°C |
| **Ni-O** | R (Å) | 2.09 | 2.01 | 2.04 | 2.04 | 2.05 |
| | N | 6.0 | 6.0 | 4.7 | 3.1 | 3.0 |
| | $\sigma^2$ (x$10^{-3}$) | - | 3.0 | 1.0 | 1.0 | 1.8 |
| **Ni-Ni** | R (Å) | 2.95 | 2.89 | 2.95 | 2.95 | 2.95 |
| **(NiO)** | N | 12.0 | 12 | 11.3 | 7.6 | 6.8 |
| | $\sigma^2$(x$10^{-3}$) | - | 9.9 | 7.2 | 7.5 | 7.6 |
| **Ni-Ni** | R (Å) | 2.49 | - | - | 2.50 | 2.51 |
| **(Ni metal)** | N | 12.0 | - | - | 3.0 | 2.9 |
| | $\sigma^2$(x$10^{-3}$) | - | - | - | 5.6 | 8.0 |

**Reference [62]